

BULLETIN N° 237
ACADÉMIE EUROPEENNE
INTERDISCIPLINAIRE
DES SCIENCES
INTERDISCIPLINARY EUROPEAN ACADEMY OF SCIENCES



Lundi 9 septembre à 16h30
à l'Institut Curie, salle Joliot,
11-13, rue Pierre et Marie Curie 75005 PARIS/Métro : RER Luxembourg

Conférence :

*" Il y a plus de marge de manœuvre en bas de l'échelle:
vers un détecteur universel des interactions moléculaires "*

Par Terence STRICK

Directeur de recherche au CNRS,
Professeur et chef d'équipe Nanomanipulation de biomolécules
Institut Jacques Monod Université Paris Diderot et Institut de Biologie de l'ENS (IBENS)

Notre Prochaine séance aura lieu le lundi 7 octobre 2019 à 16h30
à l'Institut Curie, Amphi BURG salle annexe 2
12, rue Lhomond 75005 PARIS
Métros: Maubert Mutualité/Cardinal Lemoine (ligne 10)

Elle aura pour thème

Conférence:

*"Organisation spatiale et temporelle à l'échelle mésoscopique
d'une protéine de signalisation cellulaire "*

par Mathieu COPPEY Directeur de Recherche CNRS
Chef d'équipe Imagerie et contrôle de l'organisation cellulaire (LOCCO)
UMR168 – Laboratoire Physico-Chimie Curie
INSTITUT CURIE 20 rue d'Ulm, 75248 Paris Cedex 05

ACADÉMIE EUROPÉENNE INTERDISCIPLINAIRE DES SCIENCES INTERDISCIPLINARY EUROPEAN ACADEMY OF SCIENCES

PRÉSIDENT : Pr Victor MASTRANGELO
VICE PRÉSIDENT : Pr Jean-Pierre FRANÇOISE
VICE PRÉSIDENT BELGIQUE(Liège):
 Pr Jean SCHMETS
VICE PRÉSIDENT ITALIE(Rome):
 Pr Ernesto DI MAURO
SECRÉTAIRE GÉNÉRALE : Irène HERPE-LITWIN
TRÉSORIÈRE GÉNÉRALE: Édith PERRIER

MEMBRES CONSULTATIFS DU CA :
 Gilbert BELAUBRE
 François BÉGON
 Bruno BLONDEL
 Michel GONDRAN

PRÉSIDENT FONDATEUR : Dr. Lucien LÉVY (†)
PRÉSIDENT D'HONNEUR : Gilbert BELAUBRE

CONSEILLERS SCIENTIFIQUES :
SCIENCES DE LA MATIÈRE : Pr. Gilles COHEN-TANNOUJJI
SCIENCES DE LA VIE ET BIOTECHNIQUES : Pr Ernesto DI MAURO

CONSEILLERS SPÉCIAUX:
ÉDITION: Pr Robert FRANCK
RELATIONS EUROPÉENNES :Pr Jean SCHMETS
RELATIONS avec AX: Gilbert BELAUBRE
RELATIONS VILLE DE PARIS et IDF:
 Michel GONDRAN et Claude MAURY
MOYENS MULTIMÉDIA et UNIVERSITÉS: Pr Alain CORDIER
RECRUTEMENTS: Pr. Sylvie DERENNE
SYNTHÈSES SCIENTIFIQUES: Jean-Pierre TREUIL
MÉCENAT: Pr Jean Félix DURASTANTI
**GRANDS ORGANISMES DE RECHERCHE NATIONAUX ET
 INTERNATIONAUX**: Pr Michel SPIRO
THÈMES ET PROGRAMMES DE COLLOQUES: Pr Jean SCHMETS

SECTION DE NANCY :
PRESIDENT : Pr Pierre NABET

septembre 2019

N°237

TABLE DES MATIERES

p. 03 Séance du 9 septembre 2019 :

p. 05 Documents

Prochaine séance : lundi 7 octobre 2019

Conférence:

***"Organisation spatiale et temporelle à l'échelle mésoscopique
 d'une protéine de signalisation cellulaire "***

par Mathieu COPPEY Directeur de Recherche CNRS

Chef d'équipe Imagerie et contrôle de l'organisation cellulaire (LOCCO)

UMR168 – Laboratoire Physico-Chimie Curie

INSTITUT CURIE 20 rue d'Ulm, 75248 Paris Cedex 05

Académie Européenne Interdisciplinaire des Sciences
 Siège Social : 5 rue Descartes 75005 Paris
 Nouveau Site Web : <http://www.science-inter.com>

ACADEMIE EUROPEENNE INTERDISCIPLINAIRE DES SCIENCES

Fondation de la Maison des Sciences de l'Homme, Paris.

Séance du Lundi 9 septembre 2019/IHP 16h30

La séance est ouverte à 16h **sous la Présidence de Victor MASTRANGELO** et en la présence de nos Collègues Gilbert BELAUBRE, Jean BERBINAU, Jean-Louis BOBIN, Eric CHENIN, Gilles COHEN-TANNOUDI, Jean-Félix DURASTANTI, Claude ELBAZ, Michel GONDRAN, Irène HERPE-LITWIN, Claude MAURY, Marie-Françoise PASSINI, Edith PERRIER, Jean SCHMETS, Jean-Pierre TREUIL .

Etait également présent notre collègue, membre correspondant Benoît PRIEUR.

Etaient excusés :François BEGON, Jean BERBINAU, Jean-Pierre BESSIS, Bruno BLONDEL, Michel CABANAC, Alain CARDON, Juan-Carlos CHACHQUES, Alain CORDIER , Daniel COURGEAU, Sylvie DERENNE, Ernesto DI MAURO, Françoise DUTHEIL, Vincent FLEURY, Robert FRANCK, Jean -Pierre FRANCOISE, Dominique LAMBERT, Pierre MARCHAIS, Anastassios METAXAS, Jacques NIO, Pierre PESQUIES, Jacques PRINTZ, Denise PUMAIN, René PUMAIN, Michel SPIRO, Alain STAHL, Jean-Paul TEYSSANDIER, Jean VERDETTI.

I. Conférence de Terence STRICK

A. Présentation du conférencier par notre Président Victor MASTRANGELO

Le Professeur Terence STRICK a eu la carrière universitaire ci-dessous:

1999 : Doctorat de biologie cellulaire et moléculaire , Université Pierre et Marie Curie
 2000-2004: Post Doc indépendant à la tête d'une équipe au Cold Stream Harbor Laboratory, Cold Stream Harbor Etats Unis
 2004-2016: Chef d'Equipe Nanomanipulation des Molécules/ Institut Jacques Monod Paris
 2004-2016: Chargé de Recherche CR1 , puis Directeur de Recherche au CNRS
 2008 : Habilitation à diriger des recherches (HDR) Université Paris Diderot
 Depuis 2016: Professeur de 1ère classe , ENS Paris, Chef d'équipe à l'Institut de Biologie de l'ENS (IBENS)

Il a obtenu les récompenses suivantes en tant que chercheur::

2008 : European Young Investigator Award (EURYI), European Science Foundation
 2013 : Prime d'Excellence scientifique du CNRS
 2017 : Prime Coups d'élan pour la recherche française

L'équipe de Terence Strick déploie des techniques innovantes de **manipulation de molécules uniques** pour comprendre comment les cassures de l'ADN sont réparées par des protéines .

Les progrès de la biophysique permettent aujourd'hui d'observer en temps réel le comportement de molécules individuelles: comment elles se rencontrent , interagissent puis se séparent : une plongée dans les rouages intimes du vivant qui donne à comprendre une infinité de mécanismes.

Le projet de Terence Strick, pionnier de la **manipulation de molécules uniques**, vise à détailler les **processus de la réparation de l'ADN**. Cette fonction essentielle répond aux dommages effectués par des facteurs tels que les UV, les rayons X ou encore l'absorption de cancérogènes dans la fumée de cigarette. La réparation de l'ADN nécessite le travail simultané d'un grand nombre de protéines. Celles-ci ne sont pas en mesure de se rechercher les unes les autres et pourtant, la réparation est efficace. L'équipe de Terence STRICK, utilisant des techniques novatrices permettant simultanément de manipuler et voir des molécules individuelles, étudiera l'assemblage, l'activité et le désassemblage des complexes de réparation qui s'organisent autour d'une cassure de l'ADN rendant possible sa réparation.

B. Conférence

Résumé de la conférence:

Il y a plus de marge de manœuvre en bas de l'échelle: vers un détecteur universel des interactions moléculaires

Depuis maintenant plusieurs décennies des outils biophysiques ont permis aux chercheurs de manipuler et observer en temps réel les réactions biologiques ayant lieu à l'échelle du réactif moléculaire individuel. Avec un pouvoir de résolution qui atteint littéralement l'échelle allant de l'Angstrom au nanomètre qui est celle des liaisons et des molécules individuelles, le dénommé domaine de la " biophysique des molécules individuelles" a depuis fourni aux biologistes et aux physiciens une vision sans précédent sur la manière dont les moteurs et les machines biologiques s'assemblent et se désassemblent pour permettre à nos cellules de vivre et de fonctionner correctement. Dans cette présentation nous fournirons une vue d'ensemble historique du domaine et nous montrerons comment il a altéré notre compréhension de la structure, de la fonction et de l'organisation moléculaire et cellulaire, par exemple dans des processus clés tels que l'expression et la réparation des gènes. En retour, ces idées nous ont permis de voir sous un nouveau jour les biomatériaux et de commencer à les assembler dans de nouvelles voies permettant de générer de nouvelles et utiles fonctionnalités et mesures. Nous expliquons ceci grâce au développement d'une nouvelle catégorie de détecteurs moléculaires avec des applications au dépistage, à la caractérisation et au perfectionnement des médicaments

Un compte-rendu rédigé par un membre de l'AEIS sera prochainement disponible sur le site de l'AEIS <http://www.science-inter.com>.

REMERCIEMENTS

Nous tenons à remercier vivement M. Jean-Louis DUPLOYE et M. Yann TRAN de l'Institut Curie pour la qualité de leur accueil.

Documents

Pour préparer la conférence du Pr Mathieu COPPEY, nous vous proposons :

- p.07: un résumé de sa conférence " *Organisation spatiale et temporelle à l'échelle mésoscopique d'une protéine de signalisation cellulaire* "
- p.12 : Un article issu de la revue Cell Reports 21, 1922–1935, November 14, 2017 intitulé " **Gradients of Rac1 Nanoclusters Support Spatial Patterns of Rac1 Signaling** " accessible sur le site: <https://doi.org/10.1016/j.celrep.2017.10.069>
- p.27 : Un article issu de la revue NATURE COMMUNICATIONS | (2018) 9:4816 | DOI: 10.1038/s41467-018-07286-8 intitulé " **Optogenetic dissection of Rac1 and Cdc42 gradient shaping** " accessible sur le site: DOI: 10.1038/s41467-018-07286-8(www.nature.com/naturecommunications)

Organisation spatiale et temporelle à l'échelle mésoscopique d'une protéine de signalisation cellulaire

par Mathieu COPPEY Directeur de Recherche CNRS

Chef d'équipe Imagerie et contrôle de l'organisation cellulaire (LOCCO)

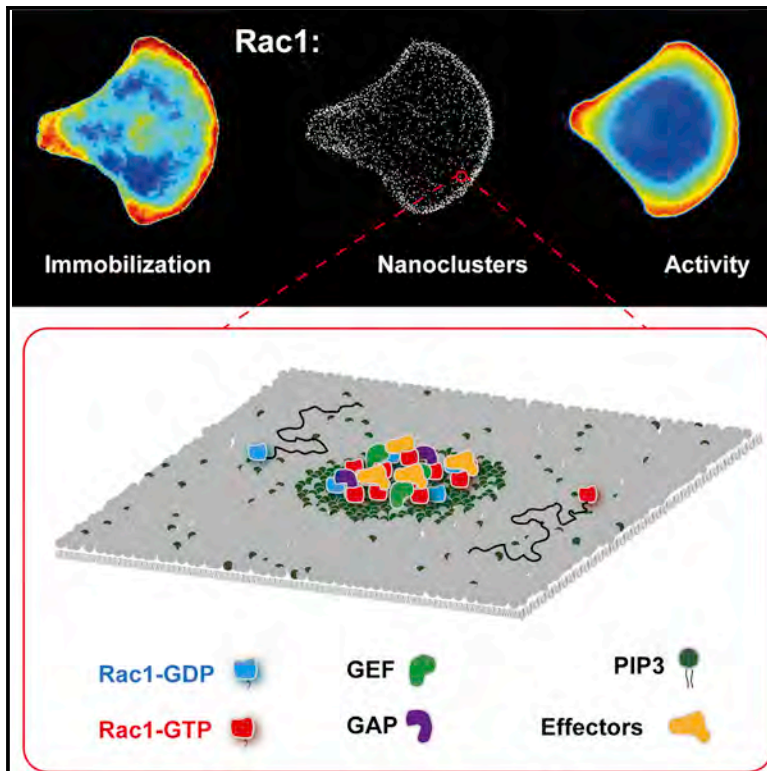
UMR168 – Laboratoire Physico-Chimie Curie

INSTITUT CURIE 20 rue d'Ulm, 75248 Paris Cedex 05

La description et la compréhension des états de la matière à l'échelle mésoscopique dans les systèmes biologiques représentent un des grands enjeux de la biophysique actuelle pour deux principales raisons. Du point de vue fondamental, cette échelle est celle de la transition entre le chaos moléculaire -les molécules soumises à l'agitation thermique effectuent des processus aléatoires- et les premières structures organisées – les molécules forment des assemblages robustes dont la fonction est déterministe-. Du point technique, cette échelle est longtemps restée inaccessible à l'observation, la microscopie optique étant intrinsèquement limitée à une résolution de l'ordre de 200 nanomètres. Après avoir introduit l'échelle mésoscopique en biologie cellulaire, j'illustrerai cet enjeu en présentant nos résultats obtenus sur une protéine de signalisation, la protéine Rac1. La signalisation cellulaire consiste en des cascades de réactions biochimiques qui permettent à la cellule de se réguler, de sentir son environnement et d'agir en conséquence. En utilisant des techniques de molécule unique pour la microscopie de super-résolution et des techniques d'optogénétique, nous avons pu montrer que la protéine Rac1 forme des agrégats nanoscopique de composition hétérogène. La distribution asymétrique de ces agrégats en gradients subcellulaire contrôle les processus cellulaires tels que la migration. Le concept qui émerge de ces résultats ainsi que ceux de la communauté, est que les objets moléculaires en biologie s'organisent et interagissent collectivement. L'idée d'interaction stéréospécifique, ou plus communément « clef-serrure » doit être étendue à une nouvelle physique qui intègre les effets collectifs reposant sur des interactions multivalentes de basses affinités.

Gradients of Rac1 Nanoclusters Support Spatial Patterns of Rac1 Signaling

Graphical Abstract



Authors

Amanda Remorino, Simon De Beco, Fanny Cayrac, ..., Jean-Baptiste Masson, Maxime Dahan, Mathieu Coppey

Correspondence

mathieu.coppey@curie.fr

In Brief

Rac1 is a small GTPase protein controlling the polymerization of actin at the front of migrating cells. Using super-resolution microscopy, Remorino et al. show that Rac1 forms nanoclusters of heterogeneous composition, which presumably act as discrete signaling platforms. The subcellular distribution of Rac1 nanoclusters follows its pattern of activation.

Highlights

- 20% of membrane-bound Rac1 forms immobile nanoclusters of ~50–100 molecules
- Nanoclusters are formed thanks to Rac1 polybasic tail and PIP2/PIP3 charged lipids
- Interaction of Rac1 with GEF/GAP/effector partners enriches nanoclusters locally
- The distribution of Rac1 nanoclusters follows the pattern of Rac1 activity



Gradients of Rac1 Nanoclusters Support Spatial Patterns of Rac1 Signaling

Amanda Remorino,¹ Simon De Beco,¹ Fanny Cayrac,¹ Fahima Di Federico,¹ Gaetan Cornilleau,¹ Alexis Gautreau,² Maria Carla Parrini,³ Jean-Baptiste Masson,^{4,5} Maxime Dahan,¹ and Mathieu Coppey^{1,6,*}

¹Laboratoire Physico-Chimie, Institut Curie, CNRS UMR168, Paris-Science Lettres, Université Pierre et Marie Curie-Paris 6, 75005 Paris, France

²Ecole Polytechnique, Université Paris-Saclay, CNRS UMR7654, 91120 Palaiseau, France

³Institut Curie, Centre de Recherche, Paris Sciences Lettres, ART Group, Inserm U830, Paris 75005, France

⁴Decision and Bayesian Computation, Institut Pasteur, 25 Rue du Docteur Roux, Paris, 75015, France

⁵Bioinformatics and Biostatistics Hub - C3BI, USR 3756 IP CNRS, Paris, France

⁶Lead Contact

*Correspondence: mathieu.coppey@curie.fr

<https://doi.org/10.1016/j.celrep.2017.10.069>

SUMMARY

Rac1 is a small RhoGTPase switch that orchestrates actin branching in space and time and protrusion/retraction cycles of the lamellipodia at the cell front during mesenchymal migration. Biosensor imaging has revealed a graded concentration of active GTP-loaded Rac1 in protruding regions of the cell. Here, using single-molecule imaging and super-resolution microscopy, we show an additional supramolecular organization of Rac1. We find that Rac1 partitions and is immobilized into nanoclusters of 50–100 molecules each. These nanoclusters assemble because of the interaction of the polybasic tail of Rac1 with the phosphoinositide lipids PIP2 and PIP3. The additional interactions with GEFs and possibly GAPs, downstream effectors, and other partners are responsible for an enrichment of Rac1 nanoclusters in protruding regions of the cell. Our results show that subcellular patterns of Rac1 activity are supported by gradients of signaling nanodomains of heterogeneous molecular composition, which presumably act as discrete signaling platforms.

INTRODUCTION

Cell migration and tissue invasion have important roles in cancer metastasis and embryonic development. Among the different mechanisms of migration, protrusion-based mesenchymal migration involves the formation of structures called lamellipodia that alternate between protruding and retracting cycles through actin polymerization and depolymerization (Krause and Gautreau, 2014). The regulation of this highly dynamic and adaptable mechanism of motion dictates the outcomes of many cellular processes. For example, the stiffness of the branched actin network (Bieling et al., 2016), the frequency of its oscillations (Mendoza et al., 2015), the relative ratio of elongation and branching (Bisi et al., 2013), and membrane trafficking (Gautier et al., 2011) can be tuned to yield

distinct phenotypic effects. This regulation is achieved through a complex coordination of many signaling pathways in which RhoGTPases, small molecular switches that integrate multiple inputs to orchestrate the dynamics of the cytoskeleton, play a pivotal role.

One of the most studied RhoGTPases, Rac1, is at the core of signaling pathways regulating cell polarization and migration. Rac1 is activated and deactivated at the plasma membrane, and possibly at endomembranes, through the interaction with guanine nucleotide exchange factors (GEFs) and GTPase-activating proteins (GAPs), respectively. Rac1 shuttles to and from the plasma membrane through its interaction with Rho GDP-dissociation inhibitors (GDIs), which mask its prenyl group. Rac1 presents spatiotemporal patterns of activity (Pertz, 2010; Machacek et al., 2009) that extend over a few micrometers and last for a few minutes during cell migration (Fritz and Pertz, 2016). Localized shuttling of Rac1 by GDIs and localized activation by GEFs are two mechanisms capable of producing and maintaining activation profiles. They represent different layers of regulation, and their relative importance is still not clear (Woods et al., 2015; Hodgson et al., 2016).

Modeling studies (Bement et al., 2006) have identified three main variables controlling the spatiotemporal properties of its subcellular gradients of activation: the spatial distribution of activators and deactivators (GEFs and GAPs, respectively), the cycling rates between activation states, and the diffusivity of RhoGTPases at the membrane. Assuming a sharply localized GEF and a uniform GAP distribution, the spatial extent of active Rac1 simply depends on its lifetime in the GTP-bound state and its lateral diffusion coefficient. Yet we do not know whether the spatial extent of Rac1 activity gradients in the cell, generated by a specific distribution of activators and deactivators, is maintained because of low mobility or short lifetimes. Some of the mechanisms that localize GEFs and GAPs have been identified and described (reviewed by Fritz and Pertz, 2016). Lipid-interaction domains with varying lipid specificity, BAR domains, tyrosine kinases, scaffold proteins, adhesion complexes, and the cytoskeleton have been shown to selectively direct GEFs and GAPs to different plasma membrane (PM) subdomains. In contrast, only a few works have focused on the study of RhoGTPases diffusivities (Shibata et al., 2013; Chazeau et al.,

2014; Das et al., 2015) or on the determination of cycling rates (Parrini et al., 2011; Davis et al., 2013).

In addition to the molecular parameters encoding the cellular-scale patterns of Rac1 activity, there might be a supramolecular organization of Rac1 signaling not accessible by conventional microscopy. In the past decade, several studies have reported the existence of nanoclusters for membrane-bound signaling proteins (Bonny et al., 2016). It has been argued that all signaling proteins might be regulated through nanoclusters (Garcia-Parajo et al., 2014). These nanoclusters accumulate around ten proteins in less than 250 nm² areas (Wittinghofer, 2014), producing highly localized increase of concentrations that allow putative thresholds to be overcome. As such, their assumed function is to ensure the transduction of signals with high fidelity, each nanocluster acting as discrete signal processing units digitalizing the input (Harding and Hancock, 2008). The small G protein Ras presents the best-studied case of nanoclustering (Wittinghofer, 2014). On the plasma membrane, about 44% of Ras proteins are organized into ~9 nm nanoclusters composed of four to seven proteins and having a 0.1–1 s lifetime (Hancock and Parton, 2005). Active and inactive forms of Ras are segregated into different nanoclusters. Ras proteins exist in different isoforms: H-Ras, N-Ras, and K-Ras. They differ in their lipid anchors and yield nanoclusters of varying acidic phospholipid, cholesterol, and scaffold protein composition. As a consequence, they behave differently when the plasma membrane is perturbed through cholesterol depletion or cytoskeleton disruptions (Zhou and Hancock, 2015), highlighting the importance of polybasic sequences in proper signal propagation (Johnson et al., 2012). In addition, positively charged membrane-anchored proteins have been shown to induce PIP2 nanoclustering by charge stabilization (Gc et al., 2016), and equivalent effects for PIP3 have been proposed (Salamon and Backer, 2013). PIP3 and PIP2 are important signaling molecules (Krause and Gautreau, 2014). Similarly, the membrane-interacting domain of Rac1 is built up of an unspecific geranylgeranyl isoprenoid lipid and a repetition of basic residues that confer specificity for the negatively charged lipids PIP2, PIP3 (Heo et al., 2006), and phosphatidylserine (Finkielstein et al., 2006; Picas et al., 2016; van den Bogaart et al., 2011). Yet despite its fundamental role, it is still unknown whether the RhoGTPase Rac1 forms nanoclusters.

In this work, we used single-molecule localization microscopy in live cells (SPT-PALM) (Manley et al., 2008) to address the architecture and dynamics of Rac1 in the basal plasma membrane of NIH 3T3 cells. We found that Rac1 displays static and diffusing states and that Rac1 immobilization is due mainly to its partitioning into nanoclusters. Rac1 immobilization and nanoclustering are enhanced at the front of the cell and correlate with regions of high Rac1 activity. The polybasic anchor of Rac1 is sufficient to drive nanocluster formation, but results obtained from Rac1 mutants show that interactions with GEFs, GAPs, and effectors are required to enrich nanoclusters at the front of the cell. Using optogenetics combined with single-molecule imaging, we causally established that activation of cycling wild-type Rac1 leads to its immobilization and that interactions with effectors are the most efficient in promoting Rac1 immobilization, similarly to what has been observed with H-Ras (Blaževič

et al., 2016). Two-color super-resolution images confirmed that nanoclusters at the active front of the cell are composed of at least Rac1, PIP3, and the WAVE nucleation-promoting factor. Additionally, by quantitatively comparing the profiles of Rac1 activity and immobilization in micro-patterned cells, we found that the fraction of Rac1 immobilization is a non-linear function of its activity, supporting the existence of an amplification mechanism by which active Rac1 is further immobilized in regions of high Rac1 activity. We propose that interactions with downstream effectors such as WAVE are responsible for this amplification by stabilizing nanoclusters and thus enhancing their lifetime.

Altogether, the heterogeneous composition of Rac1 nanoclusters suggest that they operate as signaling platforms where GEFs, GAPs, and effectors are concentrated and where the size of nanoclusters is tightly regulated by cycling between active and inactive states. Importantly, our results show that nanoclusters can be distributed as subcellular gradients. Their distribution matches the activity measured by a fluorescence resonance energy transfer (FRET) biosensor, suggesting that a supramolecular level of organization mediates Rac1 signal transduction.

RESULTS

Rac1 Forms Nanoclusters

Single-molecule tracking experiments have been used in the past to study the diffusivity of Rac1 in spreading MCF7 cells (Das et al., 2015), dendritic spines (Chazeau et al., 2014), and within focal adhesion points of HeLa cells (Shibata et al., 2013). In the present work, we used a single-particle tracking photoactivated localization microscopy (SPT-PALM) (Manley et al., 2008) approach in a total internal reflection fluorescence (TIRF) microscopy configuration. TIRF microscopy allowed us to capture only molecules present in the basal membrane without the noisy contribution of cytoplasmic proteins. The benefit of SPT-PALM approaches is to yield individual localizations in live cells that can be used both to access the supramolecular organization of molecules in the membrane and to build individual trajectories revealing the mobility of the tagged proteins, as depicted in Figure 1A. Here, we used live cells stably expressing Rac1 labeled with the photoconvertible protein mEOS2, which we sparsely photoactivated to image single molecules (Figure 1B; Movie S1). Localizations and trajectories were used to build quantitative reporters of the architecture and dynamics of Rac1 at the basal plasma membrane (Figure 1C).

A density-based representation of PALM live cell images of wild-type Rac1 tagged with mEOS2 (mEOS2-Rac1-WT) revealed that Rac1 forms nanoclusters (Figure 1D), similarly to Ras proteins (Plowman et al., 2005; Zhou and Hancock, 2015). Analysis of the spatial distribution of mEOS2-Rac1-WT using a Ripley K function (L[r]-r) (Shivanandan et al., 2015) (Figure 1E) and a pair correlation photoactivated localization microscopy (PC-PALM) approach (Veatch et al., 2012) provided quantitative supports of nanocluster formation. Ripley functions (Figure 1E) exhibit a peak at 200 nm, indicating an inhomogeneous distribution of proteins on the membrane with structures of length scales on the order of hundreds of nanometers. Moreover, fitting of the pair correlation function of mEOS2-Rac1-WT (Figure S1)

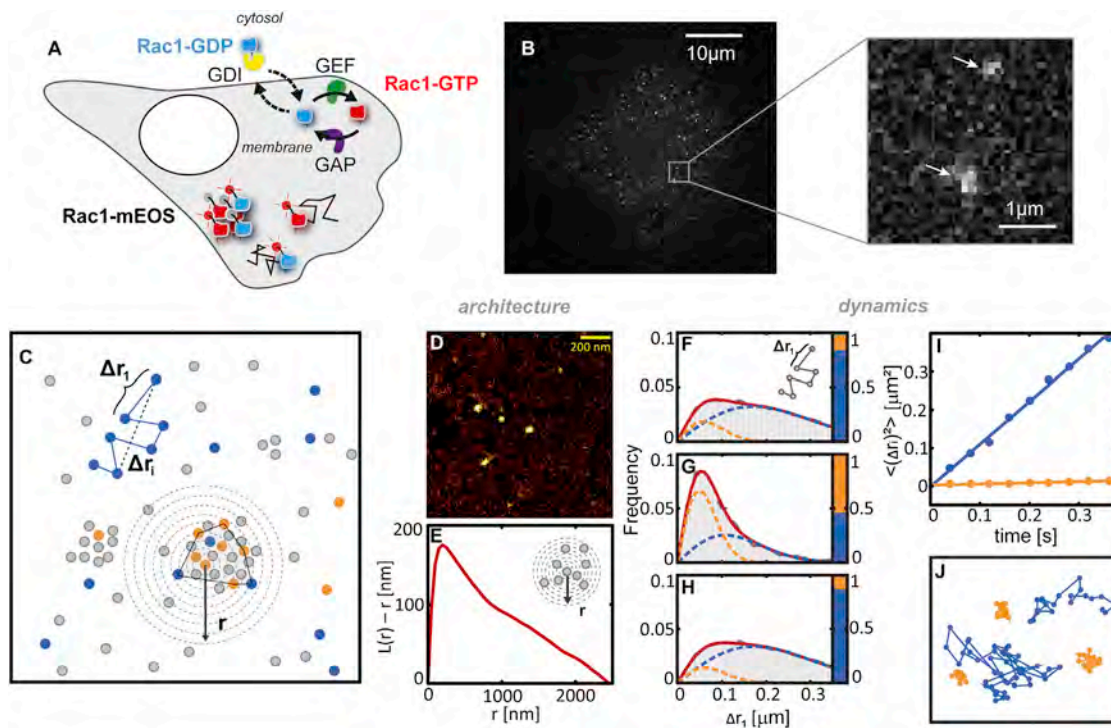


Figure 1. Rac1 Forms Nanoclusters and Presents Two Diffusive States

(A) Scheme of the mechanisms regulating Rac1 activity inside the cell. Rac1 switches between GDP (blue) and GTP (red) loaded forms and shuttles between the membrane and the cytosol. We used a TIRF SPT-PALM strategy, by fusing the photoactivatable mEOS2 fluorescent protein to Rac1. Using low power of activation, only a few mEOS2 molecules are photoconverted, giving access to localizations and trajectories of single Rac1 molecules (either GTP or GDP loaded). (B) Example of a frame from a single movie of mEOS2-Rac1-WT at the basal plasma membrane (see [Movie S1](#)) and zoom showing two individual molecules (arrows).

(C) Scheme of the parameters extracted from the single-molecule movies. Blue/orange (diffusing/immobile) spots are mEOS2 molecules that are imaged and localized from the movies. Gray spots represent mEOS2 molecules that are not imaged. From the trajectories, we extracted Δr_i , the displacement for a time lag t_i . From the localizations, we calculated the local density as a function of r , the distance from the center of a molecule (Ripley function). We identified nanoclusters using a DBSCAN algorithm. Nanoclusters were segmented using the convex hull (polygon).

(D and E) A PALM image (D) (color bar, 0–60 neighbors) of Rac1 reveals its nanocluster organization that yields a peak in the Ripley function (E).

(F–H) Single-translocation histograms (gray), Δr_i , between consecutive frames in the whole cell (F), inside nanoclusters (G), and outside nanoclusters (H) cannot be fitted with a single Brownian population. When fitted with two states, they yield a quasi-static component (orange) and a freely moving one (blue) with different population sizes. The sum of the two components is given by the red curve. Inside nanoclusters, the amount of immobilization (represented by the bar graph on the right side of plots) is much higher than outside.

(I) The mean square displacement recovered from histogram fits is linear with increasing time interval ([Figure S4](#)), and their slopes yield diffusion coefficients of $D_{\text{mobile}} = 0.28 \mu\text{m}^2/\text{s}$ for the mobile state and $D_{\text{static}} = 0.008 \mu\text{m}^2/\text{s}$ for the static state. The origin of the mobile state line yields a localization precision of $31 \pm 3 \text{ nm}$.

(J) Representative trajectories of the two populations.

Details on methods can be found in [Experimental Procedures](#).

required two components: a Gaussian one corresponding to the localization accuracy associated with multiple observations of the same molecule and an exponential one decaying over a length scale of 100–200 nm, which accounts for the existence of nanoclusters. In contrast, the pair correlation function ([Figure S1](#)) of a transmembrane domain control ([Specht et al., 2011](#)) tagged with mEOS2 can be properly fitted with only the Gaussian component. To further exclude the eventuality of spurious nanocluster identification due to the consecutive imaging of the same immobile protein, we corrected PALM images of mEOS2-Rac1-WT on fixed cells by eliminating the localizations that were within the localization precision in consecutive frames. The corrected images yielded virtually identical images than the uncorrected ones ([Figure S1](#)).

We next checked if Rac1 nanoclusters are also present for endogenous Rac1. We acquired “stochastic optical reconstruction microscopy” (STORM) images in fixed cells of immunolabeled endogenous Rac1. Resulting images also show nanoclusters ([Figure S1](#)) and show pair correlation functions that cannot be fitted solely with a Gaussian component ([Figure S1](#)). Altogether, our measurements provide strong evidence that Rac1 forms nanoclusters at the plasma membrane.

Rac1 Is Immobilized in Nanoclusters

As previously shown for Ras, nanoclusters can arrest proteins and thus modulate lateral diffusivity on the membrane. We thus assessed if nanoclusters also immobilized Rac1 molecules. We extracted trajectories of single molecules of mEOS2-Rac1-WT

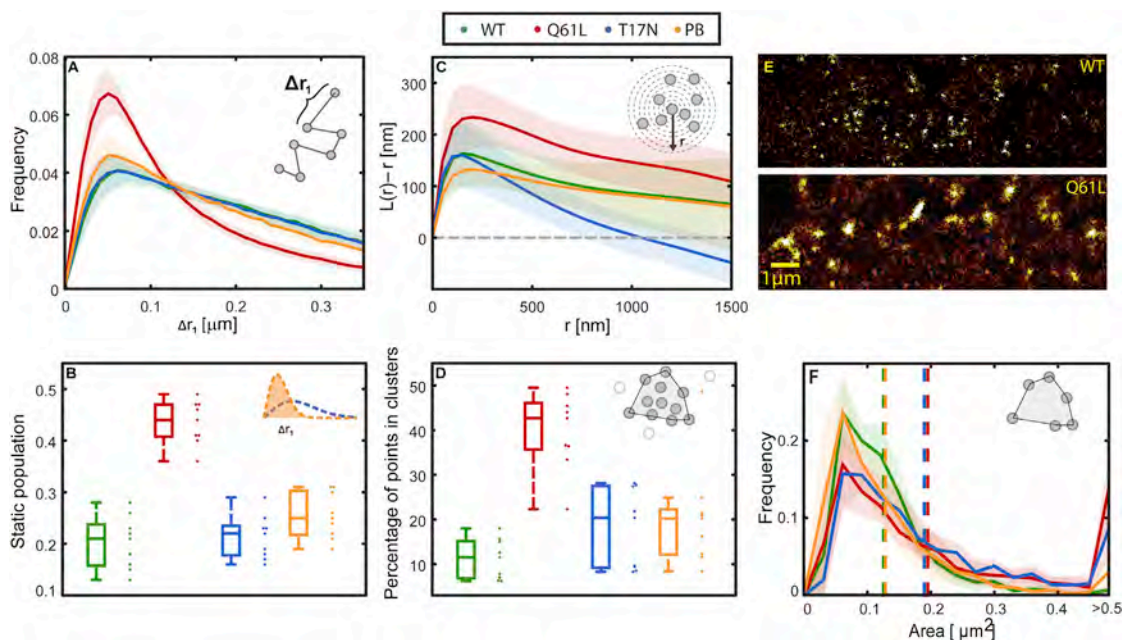


Figure 2. Active Rac1 Presents Decreased Diffusivity and Increased Nanoclustering

(A) Single-translocation histograms obtained from single-molecule movies of wild-type (mEOS2-Rac1-WT, green), active (mEOS2-Rac1^{Q61L}, red), and inactive (mEOS2-Rac1^{T17N}, blue) Rac1 mutants and the polybasic-CAAX control membrane anchor (PB-CAAX, orange). The histograms are fitted with two independent populations of different diffusivity (see [Experimental Procedures](#)).

(B) The integrated relative area of the static population obtained in (A) is larger for mEOS2-Rac1^{Q61L} than for mEOS2-Rac1-WT, mEOS2-Rac1^{T17N}, and the polybasic-CAAX membrane anchor, showing that the degree of immobilization increases with Rac1 activity.

(C) The peak in the Ripley function $L(r)-r$, measuring the degree of Rac1 nanoclustering, is higher for mEOS2-Rac1^{Q61L}, showing that increasing activity of Rac1 produces, as well, higher nanoclustering.

(D) The ratio of points contained within nanoclusters obtained with a DBSCAN algorithm is more than twice as large for mEOS2-Rac1^{Q61L}.

(E) PALM images (color bar, 0–60 neighbors) of representative nanoclusters of mEOS2-Rac1-WT (top) and mEOS2-Rac1^{Q61L} (bottom) exhibit a significant difference in nanocluster sizes.

(F) Mean nanocluster surface areas shown in dashed lines are larger for mEOS2-Rac1^{Q61L} and mEOS2-Rac1^{T17N}. Note that the last point of all curves increases as it contains all residual values greater than $0.5 \mu\text{m}^2$.

(A) and (F) are means of nine different single-cell histograms, and error bars are calculated as SDs. The mean Ripley function in (B) is a mean of nine different single-cell Ripley functions with error bars calculated as SDs. Boxplots in (B) and (D) represent the medians of measurements on nine different cells.

(see [Experimental Procedures](#)) and built histograms of the displacements of molecules between consecutive frames (Figures 1F–1H), called single translocations hereafter. Such histograms could not be fitted with a model of a single Brownian species and required two populations (Schütz et al., 1997). The analysis of the distribution of single displacements for increasing time intervals clearly supported the bimodality of the diffusion (Figures 1I and S2). The diffusivity of the slower state ($D_{\text{slow}} = 0.008 \pm 0.003 \mu\text{m}^2/\text{s}$) is within the localization precision of our experimental system and can be considered as static. In the rapid state, the diffusion coefficient is $D_{\text{fast}} = 0.28 \pm 0.003 \mu\text{m}^2/\text{s}$, in agreement with the lateral diffusion coefficient of a freely moving membrane-bound protein. Trajectories shown in Figure 1J are representative of each state of Rac1 mobility.

We looked for a preferential partitioning of the static state in nanoclusters. Nanoclusters were identified and segmented using a density-based scanning algorithm (Tran et al., 2013) such that trajectories could be sorted as belonging or not to nanoclusters (see [Experimental Procedures](#)). Histograms of single translocations in Figure 1G show that trajectories within nanoclusters present a 5-fold higher static population than those in regions

outside nanoclusters (Figure 1H). We estimated that 15% of all mEOS2-Rac1-WT immobilizations happen inside nanoclusters (Figure S2). Although this number might be largely underestimated because nanoclusters of smaller sizes are missed by our method, this result shows that partitioning into nanoclusters is one mechanism by which Rac1 becomes immobilized.

Active Rac1 Presents an Increased Fraction of Immobilization and Nanoclustering

We next assessed the relationship between activation and immobilization of Rac1 by examining the diffusivity and nanocluster partitioning of different Rac1 mutants. Figure 2A shows single-translocation histograms of mEOS2-tagged wild-type Rac1 (mEOS2-Rac1-WT), constitutively active Rac1 (mEOS2-Rac1^{Q61L}), dominant-negative Rac1 (mEOS2-Rac1^{T17N}), and the CAAX-polybasic region that works as a membrane anchor after post-translational modifications. Figure 2B shows the distribution of the static populations sizes obtained from fitting the translocation histograms (Schütz et al., 1997). Interestingly, the polybasic membrane anchor presents a similar degree of immobilization and nanoclustering as the mEOS2-Rac1-WT,

suggesting that nanocluster formation is inherent to the Rac1 CAAX-polybasic C-terminal domain of the protein. This phenomenon is consistent with previous reports on the capacity of the C-terminal polybasic domain to mediate Rac1 oligomerization (Zhang et al., 2001). However, mEOS2-Rac1^{Q61L}, which has the largest static population (Figure 2B), the highest peak in Ripley K functions (Figure 2C), and the highest percentage of localizations within clusters (Figure 2D), shows that immobilization and nanoclustering have a positive correlation with Rac1 activity. These results, together with previous reports (Shibata et al., 2013; Das et al., 2015; Chazeau et al., 2014), provide robust evidence that in migrating fibroblasts GTP-loaded active Rac1 is less mobile than its inactive counterpart.

In addition to the differences in nanocluster partitioning among Rac1 mutants, PALM images (Figure 2E) of representative nanoclusters for mEOS2-Rac1-WT and mEOS2-Rac1^{Q61L} show a clear difference in size. mEOS2-Rac1-WT displays nanocluster sizes comparable with those of the polybasic-CAAX membrane anchor, whereas mEOS2-Rac1^{T17N} and mEOS2-Rac1^{Q61L} display twice larger nanoclusters (Figure 2F). The quantification of the number of proteins per nanoclusters is a difficult task because of the blinking of mEOS2 (Durisic et al., 2014; Fricke et al., 2015). However, on average, we estimated that mEOS2-Rac1^{Q61L} and mEOS2-Rac1^{T17N} mutants present 233 ± 110 and 232 ± 49 localizations per nanoclusters, whereas mEOS2-Rac1-WT and the polybasic-CAAX anchor present 97 ± 33 and 83 ± 38 localizations. The localizations can be used as a loose estimate of the real number of molecules per nanocluster. If we consider that in our experimental conditions, a single molecule is counted on average 2.3 times and that the photophysics of mEOS2 allow sampling of only 78% of the molecules (Durisic et al., 2014), the number of molecules per nanocluster can be estimated as 0.55 times the number of localizations per nanocluster. Hence mEOS2-Rac1-WT nanoclusters are composed of approximately 50 molecules, about five times more than the number of Ras molecules in its nanoclusters (Hancock and Parton, 2005). Larger areas and larger numbers of localizations per nanoclusters present in mEOS2-Rac1^{Q61L} and mEOS2-Rac1^{T17N} mutants show that the cycling between active and inactive states is a major factor regulating nanocluster size.

Cycling rates are of high relevance in signaling. Fast cycling of Rac1, but not locking of Rac1 in its GTP-bound form, was shown to transform cells, like the oncogenic activation of upstream GEFs (Wertheimer et al., 2012; Davis et al., 2013). These results suggest that the cycling kinetics of Rac1 activation determine the transduction efficiency of Rac1 downstream signaling. Given that mEOS2-Rac1^{Q61L} is locked in its GTP-bound state, we examined whether the link between diffusivity and activity identified in mEOS2-Rac1^{Q61L} was also present in cycling Rac1. To this end, we coupled single-molecule tracking experiments with optogenetic activation (Kennedy et al., 2010) (Figure 3A). In transiently transfected cos7 cells, we illuminated for 10 min a specific region of the cell to recruit at the plasma membrane the catalytic domain of the Rac1 GEF Tiam1 (Cry2-Tiam1-iRFP), thereby inducing localized activation of Rac1. Our optogenetic activations led to a 1.2- to 2.2-fold increase of Cry2-Tiam1-iRFP inside the region of activation (Figure S3). When analyzing single-translocation histograms, we found that only mEOS2-

Rac1-WT displayed an increase in the static population size upon recruitment of Cry2-Tiam1-iRFP (Figure 3B). We acquired single-molecule movies of all mEOS2-tagged Rac1 mutants and the polybasic-CAAX anchor before and after recruitment (Figures 3C–3H), and we mapped the diffusivities over cells using a recently developed methodology (see Experimental Procedures). The polybasic-CAAX membrane anchor and mEOS2-Rac1^{T17N} cannot engage effectors, and mEOS2-Rac1^{Q61L} is already in the active state and cannot increase its interaction with effectors. Taking into account that Cry2-Tiam1-iRFP has a diffusivity of $0.1 \pm 0.03 \mu\text{m}^2/\text{s}$ (Valon et al., 2015), comparable with that of the mobile population of Rac1, we attributed the increased immobilization of mEOS2-Rac1-WT to an increase in the amount of active molecules and the consequent interaction with effectors. These optogenetic experiments show that for cycling Rac1, there is a causal relationship between activation and immobilization.

Rac1 Presents Similar Gradients of Immobilization, Nanocluster Density, and Activity

Motivated by previous studies that identified spatial profiles of RhoGTPases activity across cells (Yang et al., 2016), we aimed to compare them with immobilization profiles and nanocluster distribution. To this end, we plated cells on crossbow fibronectin micropatterns to obtain a normalized cell shape and organization (Théry et al., 2006). The “front” of these cells exhibits ruffling (Viaud et al., 2014) and mimics a lamellipodium rich in branched actin. This approach allows the comparison of several measurements taken in different experiments and offers a template for a multiplex mapping approach (Figure 4A). Because of the reduced cell-to-cell variability, we were able to average and map in the same referential the fraction of immobile molecules, the nanocluster densities, and the FRET ratiometric images (Figures 4B–4F).

We first acquired single-molecule movies (2,000–5,000 frames at 25 Hz) with densities comparable to Figure 1B ($0.2 \text{ molecules}/\mu\text{m}^2$). We then mapped Rac1 diffusivity in 9–18 individual cells for each mutant, and we averaged those maps (Figure 4B) after morphing each cell onto the average shape (see Experimental Procedures). mEOS2-Rac1-WT, mEOS2-Rac1^{Q61L}, and mEOS2-Rac1^{T17N} exhibit diffusivity gradients from the front to the middle of the cell with a region of lowest diffusivity along the cell front-most region. mEOS2-Rac1^{Q61L} presents the greatest contrast in diffusivity between front and middle. Because a given local average diffusion coefficient corresponds to a given local proportion of immobile molecules, diffusivity maps can be interpreted in terms of local fraction of immobilization (see color bar in Figures 4B and 4D). By taking into account the diffusion constant of the slow and fast states derived from tracking experiments, average diffusivities $D_{\text{mean}} = f_i \cdot D_{\text{slow}} + (1 - f_i) \cdot D_{\text{fast}}$ yielded immobilization fractions f_i . In the same single-molecule movies, nanoclusters were identified, and their spatial densities mapped onto the cell (see Experimental Procedures). As expected given our previous results, the nanocluster density map in Figure 4C shows that mEOS2-Rac1-WT, mEOS2-Rac1^{Q61L}, and mEOS2-Rac1^{T17N} present nanocluster enrichment at the front of the cell, supporting again the link between nanocluster partitioning and immobilization.

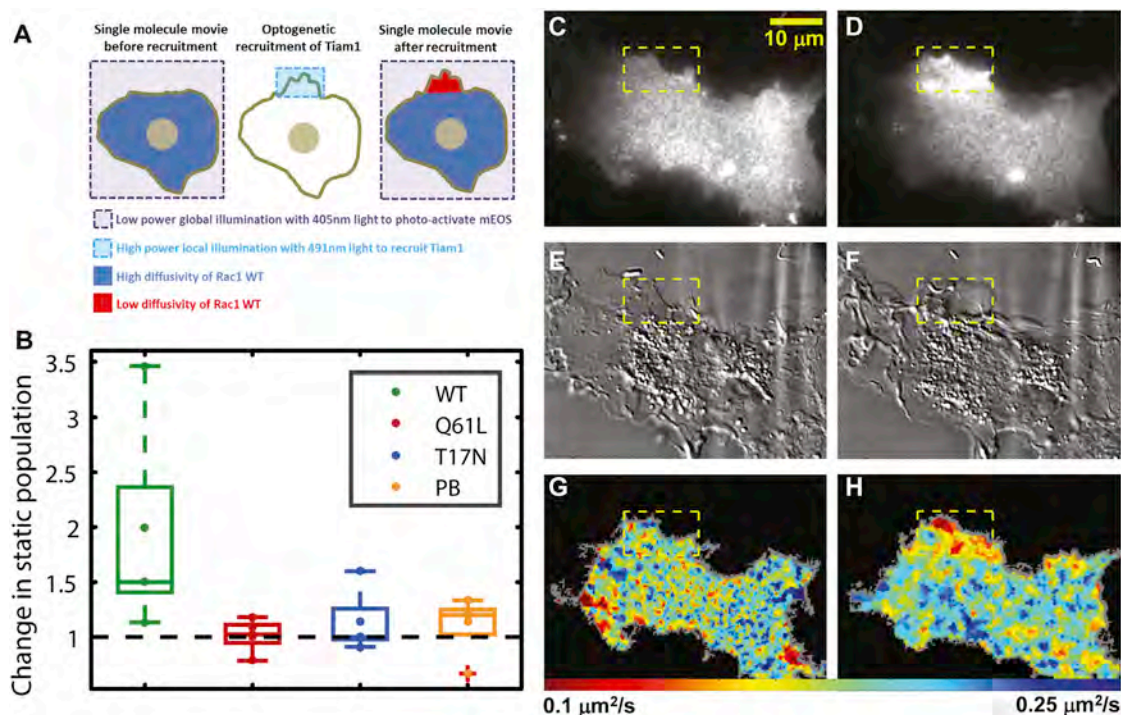


Figure 3. Diffusivities as a Function of Rac1 Activity Modulated through Optogenetics

(A) Schematic of the experiment. (Left) A single-molecule movie is acquired by photoconverting mEOS2-Rac1 with low global 405 nm illumination to avoid significant optogenetic recruitment. (Middle) A 10 min local recruitment step is performed, and higher power 491 nm light is used to illuminate a region of interest and recruit Tiam1, a GEF of Rac1, with local specificity. (Right) Another single-molecule movie is acquired.

(B) Initial and final single-molecule movies were localized and tracked to yield single-translocation histograms as shown in Figure 1. The ratio of the static population within the activation region between the final and initial movie shows an increase of the immobilization upon optogenetic activation only for mEOS2-Rac1-WT.

(C–F) iRFP channel images before (C) and after (D) optogenetic activation show Tiam1 recruitment efficiency, and DIC images before (E) and after (F) optogenetic activation expose ruffling induced by Tiam1 recruitment.

(G and H) Diffusivity maps before (G) and after (H) optogenetic activation exhibit immobilization of mEOS2-Rac1-WT confined to the activation region. Seven cells were used for each condition.

We also measured the Rac1 activity map on crossbow micro-patterns with a FRET biosensor (Moshfegh et al., 2014). Assuming that the distribution of the inactive Rac1 is uniform, as suggested by the large pool of inactive Rac1, the pixel intensities in ratiometric FRET images are proportional to the local amount of active Rac1. Under this assumption, the FRET signal provides a linear measure of the relative Rac1 activity. The nanocluster distribution and diffusion map of the WT (Figures 4D and 4E) match the biosensor signal (Figure 4F), all showing a decaying gradient from the front to the center. Thus, in an unperturbed condition, we see a clear positive correlation between Rac1 activity, immobilization, and nanocluster density.

GEF/GAP Cycling Rather Than GDI-Mediated Membrane Shuttling Regulates Rac1 Activation Patterns in Spread Cells

Localized shuttling of Rac1 to the membrane is one of the processes potentially regulating Rac1 activation. The relative weight of local activation versus local delivery in cell polarity establishment has been addressed before for *cdc42* (Woods et al., 2015; Hodgson et al., 2016). Localized delivery has been pro-

posed as a critical mechanism in the establishment of cell polarity in cells minutes after attachment (Das et al., 2015). Yet the importance of localized delivery may differ in the context of already spread cells. It has been shown that the attachment and spreading processes involve a particular set of signaling pathways (Schwartz, 1997), which may not be triggered once cells have reached a steady state. To evaluate the role of localized delivery in the context of already spread cells, we performed a plasma membrane turnover analysis on the basis of photobleaching experiments.

Fluorescence recovery after photobleaching (FRAP) experiments of the green form of mEOS2-Rac1-WT on the whole basal membrane with TIRF microscopy showed that the shuttling of Rac1 to the membrane slows down along the spreading process. By performing FRAP experiments 30 min and 3 hr after plating, we found that fluorescence recovery times increased from about 6 to about 20 min (Figure S4). A turnover time of 20 min in fully spread cells is of the same order of magnitude as the plasma membrane recycling. This experiment shows that GDI-mediated shuttling occurs on a longer timescale than protrusion/retraction cycles. Therefore, we considered that the

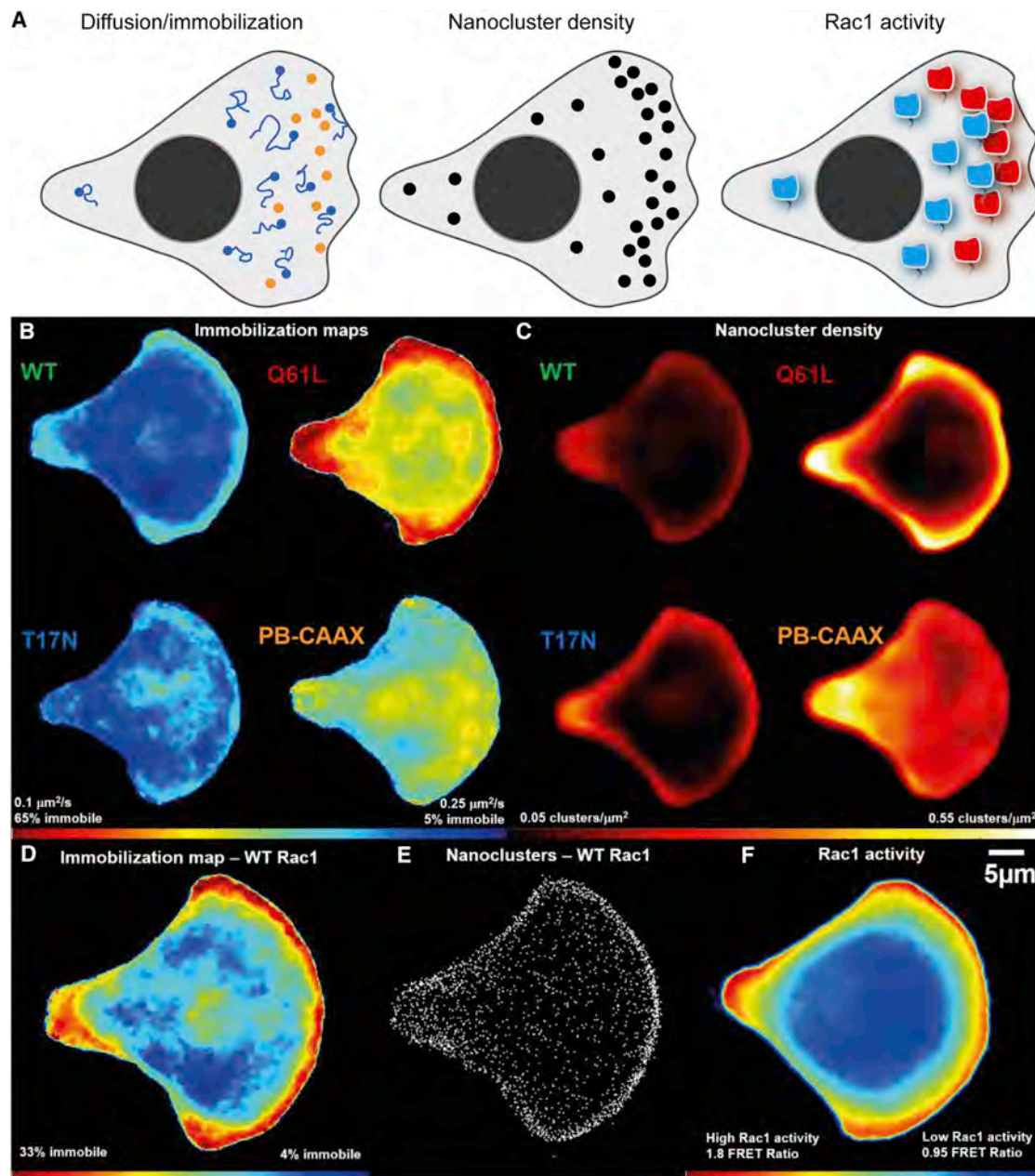


Figure 4. Rac1 Diffusivity, Activity, and Nanocluster Distribution along Normalized Polarized Cell States Imposed by Fibronectin Crossbow Micro-Patterns

(A) Cartoon describing the three parameters presented in this figure.

(B) Immobilization/diffusion maps were obtained from 9 cells per mutant and 18 cells for the mEOS2-Rac1-WT. Cells were tessellated with a Voronoi mesh, the local diffusion coefficient in each region was estimated from the single-molecule localizations using an inference approach (see [Experimental Procedures](#)), and cells were wrapped onto the average cell shape and averaged (see [Experimental Procedures](#)). Immobilization maps of Rac1 mutants show decreased overall diffusivity for mEOS2-Rac1^{Q61L} and an inhomogeneous diffusivity distribution for all three forms of Rac1, with lower diffusivity at the front and back, in contrast to the polybasic anchor, which exhibits uniform diffusivities.

(C) Nanocluster density maps (see [Experimental Procedures](#)) show a higher nanocluster density for mEOS2-Rac1^{Q61L} and an increased nanocluster density at the front of the cell for all three Rac1 mutants.

(D–F) Comparison of immobilization maps with a maximized dynamic range (D), nanocluster distribution of wild-type Rac1 (E), and Rac1 activity maps obtained from FRET biosensor ratios (F); all exhibit a gradient from front to center.

predominant mechanism for the generation and maintenance of activation profiles in our experimental conditions was the localized cycling of Rac1, not its localized delivery.

Rac1 Polybasic Tail Is Sufficient for Nanocluster Partitioning, but Interactions with Rac1 Partners Are Required for Nanocluster Enrichment in Active Regions of the Cell

To further dissect the role of Rac1 molecular interactions in regulating nanocluster distribution, we next quantified the enrichment of nanoclusters in the front of the cell for all mutants, exploiting the fact that they have distinct interacting partners. Among the Rac1 interactome, the best-characterized Rac1 partners are GEFs, GAPs, and the direct effectors. mEOS2-Rac1-WT can interact with all of them. mEOS2-Rac1^{Q61L} can interact with GAPs and effectors and perhaps also with GEFs, as demonstrated for Ras proteins (Hobbs et al., 2016). However, mEOS2-Rac1^{T17N} exhibits high affinity for GEFs but cannot bind effectors or GAPs.

To quantify the tendency of Rac1 to cluster in different parts of the cell, we divided the crossbow into three different regions, as shown in Figure 5A, and measured the density of nanoclusters (Figure 5B) and the percentage of Rac1 detections in nanoclusters for each region (Figure 5C). We chose to exclude the back of the cell from the analysis given that its morphology departs from the canonical lamellipodia. Cells plated in crossbow micropatterns present a “small front” at the back, characterized by a high concentration of cortactin (Théry et al., 2006) and high branching. In this aspect, they differ from freely migrating cells that exhibit a retracting tail.

A similar number of immobilizations as the one reported here has been seen for the polybasic-CAAX motif inside and outside of focal adhesions in HeLa (Shibata et al., 2013) and MEF (Rossier et al., 2012) cells and in dendritic spines (Chazeau et al., 2014). However, during spreading of MCF7 cells, the polybasic-CAAX anchor does not seem to present a slowly diffusing population (Das et al., 2015). Here, we identified that 18% of the polybasic-CAAX anchor of Rac1, similarly to that of H-Ras (Pezzarossa et al., 2015), is organized into nanoclusters (Figure 5C) and that 23% of the immobile population can be found within nanoclusters (Figure S4).

Yet the interactions responsible for polybasic-CAAX nanocluster formation are insufficient to enrich Rac1 nanoclusters at the front of the cell (Figure 5D). In contrast, mEOS2-Rac1-WT, mEOS2-Rac1^{T17N}, and mEOS2-Rac1^{Q61L} (Hobbs et al., 2016; Um et al., 2014) exhibit a 2-fold increase in nanocluster density at the front (Figure 5D), very likely due to additional interactions. These results suggest that GEFs, GAPs, and effectors are sufficient for a relative enrichment of Rac1 nanoclusters at the front of the cell. The significant increase of nanoclustering in mEOS2-Rac1^{Q61L} suggest additionally that interactions with effectors, strongly present in this mutant, are the most effective in promoting nanocluster partitioning.

To test this hypothesis, we looked for the presence within nanoclusters of WAVE2, a major Rac1 effector, and PIP3, which recruits GEFs and GAPs. We acquired two-color PALM/STORM images of cells expressing mEOS2-Rac1^{Q61L} and immunolabeled WAVE2 or PIP3. Supporting our hypothesis, we observed

a colocalization of mEOS2-Rac1^{Q61L} and WAVE2 (Figures 5E–5G) and a colocalization between mEOS2-Rac1^{Q61L} and PIP3 (Figures 5G and 5H) in some of the nanoclusters at the front.

Rac1 Nanoclusters Do Not Depend on the Actin Cytoskeleton

Actin has been proposed as an inducer of membrane protein nanoclusters either via the formation of transient contractile regions at the plasma membrane that stabilize liquid order domains and couple to extracellular glycosylphosphatidylinositol-anchored proteins (GPI-Aps) or through the direct interaction of transmembrane proteins with actin filaments (Raghupathy et al., 2015; Plowman et al., 2005). Indeed, nanoclusters of different Ras isoforms exhibit selective dependence on actin. Figure 5I shows that treatment with latrunculin and cocktails that freeze actin dynamics (Peng et al., 2011) does not have an effect on the diffusivity of any of the Rac1 mutants or the polybasic-CAAX anchor control. These results suggest that, like H-RasGTP (Plowman et al., 2005; Huang et al., 2013; Köster et al., 2016), Rac1 is found in nanoclusters that do not depend on the actin cytoskeleton.

Partitioning of Rac1 in Nanoclusters Is Amplified in Regions of High Rac1 Activity

To further assess the role of interactions in nanoclustering, we performed a detailed quantification of Rac1 immobilization fractions, nanocluster density, and Rac1 activity at the cell front (Figure 5J). Immobilization fraction and nanocluster density profiles can be perfectly overlaid, whereas activity gradient shows a twice-larger spatial extent (Figure 5J). Plotting the nanocluster density as a function of the activity shows a non-linear relationship between the two (Figure 5K). Immobilization fractions are constant for low Rac1 activity. However, for increasing Rac1 activity, the immobilization fraction increases drastically. This observation points to the existence of an amplification mechanism by which active Rac1 molecules have an enhanced propensity to partition into nanoclusters in regions of high Rac1 activity. Note that this amplification holds under the assumption of a linear relationship between the FRET ratio and the relative Rac1 activity (see above).

DISCUSSION

We performed a single-molecule analysis of Rac1 mobility and supramolecular architecture in migrating fibroblasts. Our main finding is that a significant fraction of Rac1 at the plasma membrane is found in nanoclusters of a few tens of molecules, which are distributed as gradients matching Rac1 subcellular patterns of activity.

Because the polybasic anchor of Rac1 forms nanoclusters and because nanocluster partitioning is independent of actin, Rac1 nanocluster formation is probably driven by electrostatic interactions of its polybasic-CAAX anchor with negatively charged lipids such as PIP2 and PIP3, as previously proposed (Li et al., 2014). Nanoclusters would form and dissociate spontaneously, without the requirement for active processes or biochemical modifications. Previous studies on the formation of nanoclusters of different Ras isoforms (Zhou and Hancock,

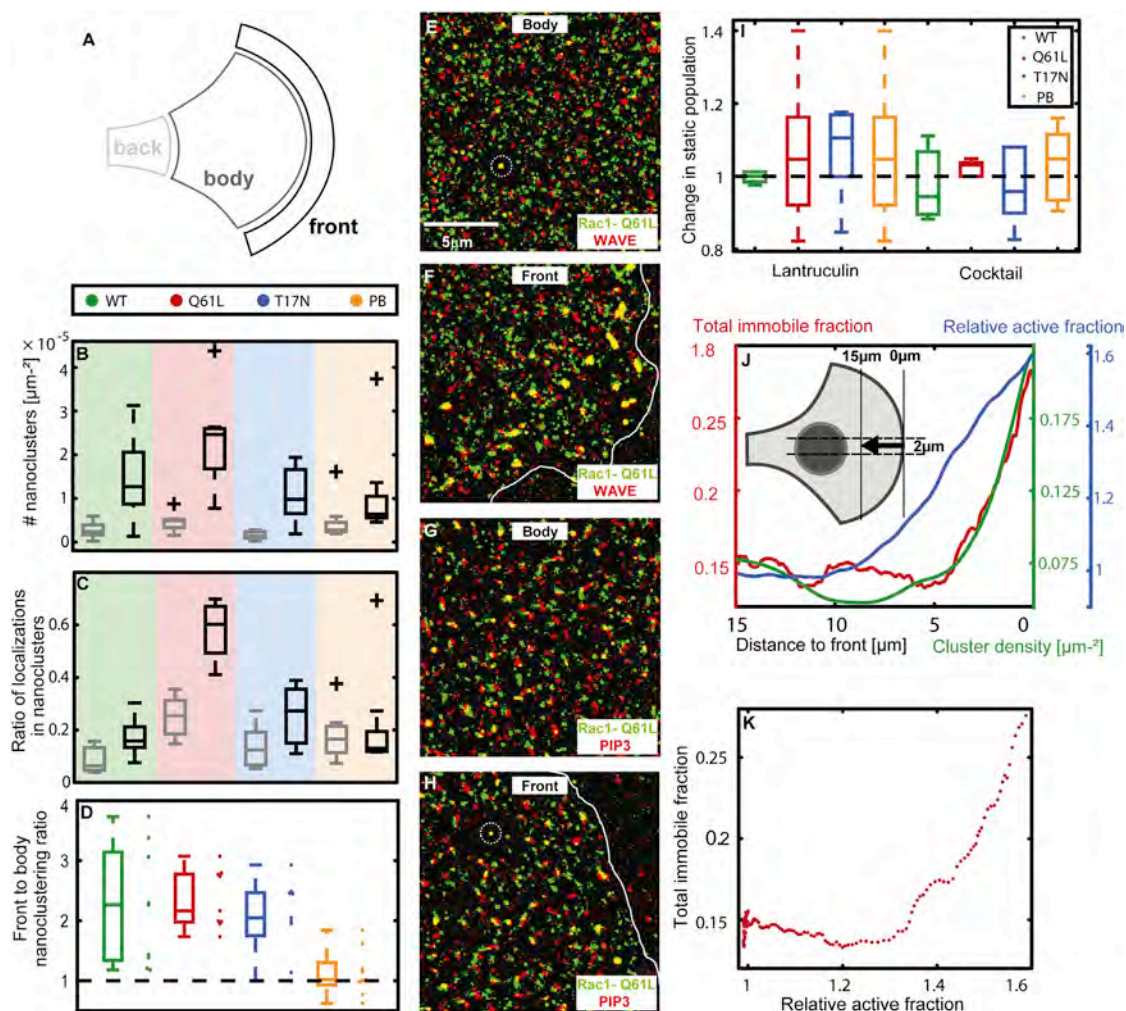


Figure 5. Rac1 Nanoclusters, Activity, Immobilization, and Composition Distribution

(A) Cells were divided into regions called front, body, and back, as depicted in the sketch.

(B and C) The number of nanoclusters per surface area (B) and the fraction of points in nanocluster (C) were measured for each region in each cell and then averaged across nine cells. Both the number of nanoclusters and the total amount of points in nanoclusters are increased at the front of Rac1 mutants in comparison with the body but are comparable for the polybasic-CAAX anchor.

(D) The front-to-body ratio of points in nanoclusters is about 2 for all Rac1 mutants and about 1 for the polybasic-CAAX anchor.

(E–H) STORM-PALM images of fixed cells plated in crossbow micropatterns expressing mEOS-Rac1^{Q61L} (green) were constructed using primary antibodies against the WAVE complex (E and F) and PIP3 (G and H), and secondary antibodies (red) tagged with Alexa Fluor 647 for front and body regions. The colocalization of mEOS-Rac1^{Q61L} and Alexa Fluor 647 is shown in yellow. mEOS-Rac1^{Q61L} and WAVE exhibit nanoclusters of high colocalization at the front of the cell but negligible colocalization in the body. mEOS-Rac1^{Q61L} also colocalizes with PIP3, but the contrast between front and body is less striking than for WAVE.

(I) In order to compare immobilization, nanoclustering, and activity profiles, we averaged 2 μm horizontal stripes across the cell center (inset) of all maps shown in Figure 4. The invariance of the static population fraction for all mutants upon treatment with either lantrunculin or a drug cocktail that freezes actin dynamics (Peng et al., 2011) suggest that the formation of Rac1 nanoclusters does not depend on actin.

(J) On the first 15 μm behind the cell edge, the profile of the Rac1 relative activity (blue) has a decay length two times larger than the profiles of Rac1 immobile fraction (red) and Rac1 nanocluster density (green).

(K) Immobilization fractions show a non-linear dependence with relative active fractions.

2015; Plowman et al., 2005) highlighted the importance of the protein anchor in signaling. These studies identified the role of cholesterol, different membrane anionic lipids, nucleotide load, degree of palmitoylation, and protein conformations in the formation and composition of Ras nanoclusters. The anchor of Rac1 resembles K-Ras in the presence of a polybasic region but rather resembles H-Ras in its mono-palmitoylation. Palmi-

toylation has been shown to induce partitioning of Rac1 into cholesterol-rich liquid-ordered regions (Navarro-Lérida et al., 2012) of sizes in the range of tenths of micrometers. One way to reconcile these data with ours is to consider that nanoclusters belong to larger structures, micrometer sized, which depend on actin and cholesterol but do not play a role in Rac1 immobilization.

Supporting the role of charged lipids in Rac1 nanoclustering, a fraction of PIP2 and PIP3 form nanoclusters in PC12 (van den Bogaart et al., 2011; Wang and Richards, 2012) and INS-1 (Ji et al., 2015) cells. These lipid nanoclusters might be segregated (Ji et al., 2015), and their diameters are 70 nm for PIP2 and 120 nm for PIP3. The spatial distribution of PIP3 and PIP2 nanoclusters was not addressed here, but other studies reported nonoverlapping distributions of PIP3 and PIP2 at the cellular scale (Petrie et al., 2009). PIP3 accumulates at the leading edge and adhesions zones during guided cell migration of fibroblasts (Haugh et al., 2000) and in membrane protrusions during random cell migration (Weiger et al., 2009). In addition, PIP3 directly recruits WAVE to the membrane of polarized cells through a basic sequence in its N-terminal part in an actin-independent manner (Oikawa et al., 2004; Lebensohn and Kirschner, 2009). Our results suggest an additional regulatory function of PIP2 and PIP3, that of inducing nanoclustering of Rac1 via the interaction with its polybasic membrane anchor through coulombic interactions (Li et al., 2014; van den Bogaart et al., 2011; Honigsmann et al., 2013).

We found that Rac1 nanoclusters are enriched at the front of the cell, contrarily to the nanoclusters of the polybasic anchor. The subcellular enrichment of nanoclusters is mediated by a second set of interactions, with the GEFs, GAPs, effectors, and possibly other Rac1 partners. In our experiments, the anisotropic spatial cue is given by the asymmetric adhesive crossbow patterns. This constraint yields an organized cell architecture with focal adhesions enriched at the adhesive borders (Théry et al., 2006) that is expected to give rise to an anisotropic distribution of GEFs and GAPs in two different ways. First, direct recruitment and activation of Rac1 to early focal adhesions, the so-called focal complexes at the lamellipodial edge, has been shown to happen via the GEFs β -Pix, DOCK180, Trio, Vav2, Tiam1, and α -Pix (Lawson and Burridge, 2014) in a cell type-dependent manner. In particular, Tiam1 accumulates at focal complexes of migrating cells, and its activation mechanisms have been elucidated (Wang et al., 2012). But also, indirect recruitment and activation of Rac1 in the proximity of focal complexes can happen via PIP3. Indeed, some Rac1 GEFs are recruited with high efficiency by PIP3, but not by other anionic lipids, because of the specificity of pleckstrin homology (PH) domains (Stahelin et al., 2014). The imposed asymmetry in fibronectin yields an intracellular anisotropy of focal adhesions and a consequent anisotropy of all the signaling components from PIP2 to PIP3, GEFs, and GAPs that results in an enrichment of cortactin at the front of crossbow micropatterns (Théry et al., 2006).

Among Rac1-interacting partners, effectors appeared to be the most effective in biasing nanocluster distribution. Indeed, mEOS2-Rac1^{O61L} presents considerably higher nanoclustering and colocalizes strongly with WAVE in super-resolution images. The importance of WAVE in promoting Rac1 nanoclustering can explain the amplification we observed in Figure 5K. Because the distribution of Rac1 effectors correlates with the local density of nanoclusters, we propose that the enrichment of nanoclusters at the front is due to an increased residence time of active Rac1 within nanoclusters rather than an enhanced seeding of nanoclusters. The amplification mechanism would then operate in the following way: active Rac1 and PIP3 (Oikawa et al., 2004;

Lebensohn and Kirschner, 2009) recruit effectors to nanoclusters that become trapped and are capable of further retaining active Rac1 within nanoclusters. As a result, this mechanism would act as Rac1 positive feedback.

In this work, we propose that nanoclusters comprising active Rac1 molecules act as signaling units regulating downstream transduction. Such nanodomains have already been observed for other membrane-bound signaling proteins, and several hypotheses have been proposed to explain their functional relevance (Cebecauer et al., 2010). High local concentrations within nanoclusters could set a threshold for signal transduction. Weak interactions can be stabilized by cooperativity in nanoclusters enabling the activation of downstream signaling cascades, as recently shown with the aPKCs kinase transducing intracellular calcium (Bonny et al., 2016). For Ras (Tian et al., 2007), it was shown that nanoclusters act as a signal-processing step converting analog inputs (concentrations of ligands) into digital ones (numbers of nanoclusters) and giving rise to other analog outputs (levels of intracellular active species) further processed downstream. The functional role of analog-to-digital-to-analog processing is not fully understood, but it has been proposed to provide high-fidelity responses (Tian et al., 2007). More recently (Roob et al., 2016), it was proposed that nanoclusters of about ten molecules exhibit optimal fidelity. Digitalization reduces the numbers of output states but also reduces the noise in the system, and a trade-off between the two maximizes information transmission.

For Rac1, we do not know yet the functional role of nanoclustering, but we can hypothesize that the same concepts hold true. Rac1 nanoclusters may work as a means to generate discrete signals by setting up WAVE thresholds that modulate actin polymerization in a non-linear way, as suggested by the need for coincident anionic lipids, phosphorylation of WAVE, and active Rac1 (Lebensohn and Kirschner, 2009). In addition, Rac1 nanoclusters may modulate reaction rates by modifying the local concentration of reactants (Groves and Kuriyan, 2010; Castellana et al., 2014), adding an additional layer of regulation aimed at refining profiles of Rac1 activity and actin polymerization. Along this line of thought, the spatial modulation of cycling rates has been observed in wound-healing experiments in oocytes (Burkel et al., 2012). Here, even if the spatial distribution of signaling molecules has already been recognized (Kholodenko et al., 2010), we show for the first time that a graded distribution of nanoclusters is a means to provide a spatially modulated digital output.

Nanoclusters can support a double role in generating high-fidelity responses. In addition to noise reduction, nanoclusters can help in the maintenance of sharp regions of signaling activity (Iyengar and Rao, 2014). Indeed, Rac1 partitioning into nanoclusters is one of the mechanisms through which Rac1 is immobilized and its diffusion spatially restricted. Previous studies (Bement et al., 2006) aimed at characterizing the link between diffusivity, cycling, and source distribution showed that decreasing the diffusion constant throughout the cell can enhance the sharpness of activity gradients. Our results show that this effect can be acting through the diffusivity gradients that follow activation profiles from the front to the back of the cell. As seen in Figure S5, immobilization gradients enable an increase in deactivation time by a factor of ~ 2 . Even though this

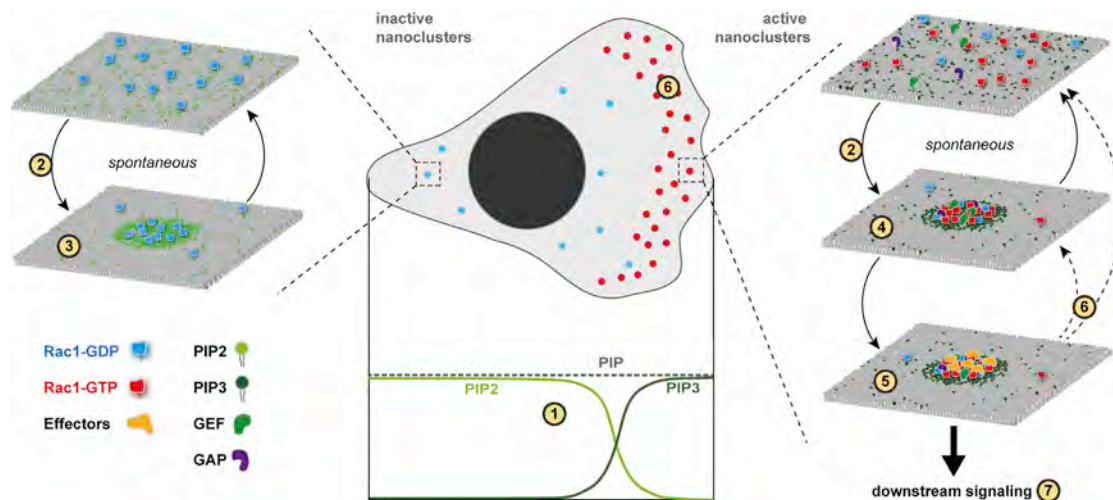


Figure 6. Model for Rac1 Nanoclustering

Opposing gradients of PIP3 and PIP2 across the cell (1) and the segregation into different clusters at the molecular level propose an enrichment of active Rac1-PIP3 nanoclusters at the front. Both active and inactive Rac1 can form nanoclusters spontaneously through electrostatic interactions (2). In the body, inactive Rac1 and PIP2 form inactive nanoclusters (3). At the front, active Rac1 and PIP3 form active nanoclusters (3), which also integrate GEFs and GAPs. These active nanoclusters recruit Rac1 effectors (5), which stabilize nanoclusters' lifetime and consequently enrich nanocluster density at the cell front (6). The heterogeneous composition of active nanoclusters suggests the existence of signaling platforms necessary for downstream signaling (7). Under this assumption, the stabilization of nanoclusters by effectors acts as positive feedback to increase the amount of Rac1 signaling where a high density of effectors is present.

might appear a mild increase, we believe that in endogenous conditions the restriction of diffusion might be a significant mechanism to maintain sharp activation gradients because the total fraction of immobile Rac1 might be higher, as suggested by the increased nanoclustering seen for endogenous Rac1 (Figure S1).

In conclusion, our findings can be summarized in the model sketched in Figure 6. Polarized migrating cells exhibit opposite gradients of PIP3/PIP2 with an enrichment of PIP3 at the front and PIP2 in the body (Petrie et al., 2009; Haugh et al., 2000; Weiger et al., 2009). Because PIP3 and PIP2 may organize in segregated nanoclusters (Wang and Richards, 2012), we believe that the front of the cell presents a larger number of PIP3 nanoclusters and the body a larger number of PIP2 ones. The affinity of the polybasic-CAAX anchor for either PIP2 or PIP3 might be comparable given that they are based on non-specific coulombic interactions, and thus nanoclusters labeled by this anchor are homogeneously distributed. However, PIP3 nanoclusters at the front recruit GEFs and GAPs and are enhancing the lifetime of Rac1 nanoclusters. Additionally, PIP3 nanoclusters and concomitant WAVE recruitment by GTP-loaded Rac1 (Oikawa et al., 2004; Lebensohn and Kirschner, 2009) further enhance nanoclusters' lifetime and nanocluster enrichment, which would consequently provide a positive feedback mechanism, sustaining cell migration.

EXPERIMENTAL PROCEDURES

Cell Culture

All single-molecule tracking, super-resolution experiments, and FRET biosensor imaging were performed on NIH 3T3 cells. Combined single-molecule tracking and optogenetics experiments were done with cos-7 cells. In

every case, cell culture was performed according to the American Type Culture Collection (ATCC) proposed protocol, cultured at 37°C in 5% CO₂ in DMEM and supplemented with 10% fetal calf serum. For single-molecule tracking and super-resolution experiments, we produced lentiviral stable cell lines expressing mEOS2-Rac1 mutants with a pHR backbone plasmid synthesized by Genescript. Cells were sorted using fluorescence-activated cell sorting. Optogenetics experiments were performed via triple transfection of CIBN-GFP (Valon et al., 2015), TIAM_linker_CRY2_IRFP obtained following the same routine as in (Valon et al., 2015), and mEOS2-Rac1 mutants using X-tremeGENE 9 and X-tremeGENE HP (Roche Applied Science, Penzberg, Bavaria, Germany) according to manufacturer's protocol. For drug treatment with the cocktail, cells were preincubated in 20 μM Y27632 for 10 min before the addition of 8 μM of jasplakinolide and 5 μM of latrunculin B. Movies were acquired ~7–12 min after the addition of jasplakinolide and latrunculin B. For the latrunculin B treatment alone, cells were incubated with 2 μM of latrunculin B, and movies were taken ~10–15 min after addition of the drug.

Cell Plating and Surface Patterning

For plating, cells were dissociated using Accutase (Life Technologies) and plated on 25 mm glass coverslips coated with fibronectin bovine protein (Life Technologies, Carlsbad, CA). Forty-nanometer-long crossbow fibronectin micro-patterned coverslips were fabricated following the protocol of Azioune et al. (2009) using PLL-g-PEG purchased from Surface Solutions Switzerland, a UV lamp (UV ozone oven 185 nm equipped with ozone catalyzer, UVO cleaner, model 342-220; Jelight), and a chrome mask (Toppan).

Single-Molecule Imaging

All experiments were imaged with a Metamorph (Molecular Devices, Eugene, OR) controlled IX71 Olympus inverted microscope, a 100× objective with NA 1.45 (Olympus, Melville, NY), and an ILAS2 azimuthal TIRF FRAP head (ilas2; Roper Scientific, Tucson, AZ) in an azimuthal TIRF configuration. Cells were kept at 37°C in 5% CO₂ with a heating chamber (Pecon; Meyer Instruments, Houston, TX). Single-molecule movies of the red form of mEOS2 were imaged at 40 ms with a 561 nm laser (Cobolt Jive 150; Hubner) of incident power of 2 kW/cm², and a BrightLine quad-edge beam splitter (Semrock Di01-R405/488/543/635). Photoconversion of mEOS2 was done with a 405 nm laser (Stradus 405; Vortran) in a TIRF configuration. Imaging of iRFP was done with a

642 nm laser (Stradus 642; Vortran) the same BrightLine dichroic, and a far-red emission filter (BLP01-635R-25; Semrock).

Analysis of Nanoclusters and Trajectories

We used the SLIMfast MATLAB code (Normanno et al., 2015) to recover single-molecule localizations and DBSCAN to identify nanoclusters. Trajectories were reconstructed by finding the optimal global assignment between points in consecutive frames using an inference approach. The mapping of diffusivities in single cells was achieved using a maximum likelihood approach. Single-cell maps were averaged using custom-built MATLAB routines. All these procedures are detailed in the [Supplemental Information](#).

Determination of Membrane Shuttling Rates

The shuttling rate of Rac1 to the membrane was analyzed using fluorescence recovery after photobleaching of the whole basal membrane of the green form of mEOS2 in TIRF mode, and recovery rates were determined as about 6 min and about 20 min (Figure S4) for spreading and spread cells, respectively.

Rac1 FRET Biosensors

We established a stable cell line of 3T3 cells expressing a Rac1-FRET-biosensor (Moshfegh et al., 2014). For imaging, cells were plated on glass coverslips with crossbow micropatterns. After 4 hr of adhesion, cells were imaged by epifluorescence using a Luca R camera (Andor on an Olympus IX71 microscope with a 60 \times magnification objective; Olympus PlanApo 60 \times , NA 1.45). The same excitation and dichroic mirrors (e.g., FF02-438/24, BS: FF-458-DiO2; Semrock) were used for the sequential acquisition of donor and acceptor images. A filter wheel was used to switch emission filters of donor (mCerulean, Em: FF01-483/32) and FRET acceptor (Em: FF01-542/27). Image processing included registration, flat-field correction, background subtraction, segmentation, and FRET/donor ratio calculations. FRET ratio images were then aligned and averaged as described in the [Supplemental Information](#).

Optogenetics

Recruitment of the catalytic domain of Tiam1 was performed using Cry2-CIBN light-gated dimerization as explained elsewhere (Valon et al., 2015). Localized recruitment was performed with 491 nm light, which is highly effective for optogenetic recruitment but less efficient for photoconversion of mEOS2. Recruitment laser pulses were applied every 10 s for 10 min. Single-molecule movies were obtained before and \sim 30 s after recruitment. The low 405 nm laser intensities used to photoconvert mEOS2 from the green to the red form did not introduce extensive global recruitment of Tiam1-Cry2-iRFP to the basal membrane. Imaging of iRFP was done with the same BrightLine dichroic and a far-red emission filter (BLP01-635R-25), and differential interference contrast (DIC) imaging was performed with a far-red filter in the illumination path to avoid CRY2 recruitment.

Immunofluorescence

Cell fixation and permeabilization were performed with 4% paraformaldehyde for 15 min and with 0.1% Triton X-100 or 0.5% NP40 for 5 min, respectively. To detect mouse WAVE2, a specific antibody called WP2 was raised against the peptide (C)NQRGSVLGPKRTS in rabbits. Specific antibodies from the rabbit serum were affinity-purified on a SulfoLink column (Pierce) displaying the same peptide. WP2 recognizes murine WAVE2 by western blot, immunofluorescence, and immunoprecipitates the WAVE complex. Anti-PIP3 was purchased from Echelon (Z-P345b) and used in a 1:100 concentration for 60 min. Goat anti-mouse and goat anti-rabbit Alexa Fluor 647-labeled secondary antibodies were purchased from Thermo Fisher Scientific (A-21236 and A-21245, respectively) and used in a 1:200 concentration for 60 min.

SUPPLEMENTAL INFORMATION

Supplemental Information includes Supplemental Experimental Procedures, six figures, and one movie and can be found with this article online at <https://doi.org/10.1016/j.celrep.2017.10.069>.

AUTHOR CONTRIBUTIONS

Conceptualization, A.R., M.D., and M.C.; Methodology, A.R., M.D., and M.C.; Software, A.R., J.-B.M., and M.C.; Formal Analysis, A.R. and M.C.; Investigation, A.R. and S.D.; Resources, F.C., F.D., G.C., and A.G.; Writing – Original Draft, A.R. and M.C.; Writing – Review & Editing, A.R., M.C., M.D., M.C.P., and A.G.; Visualization, A.R. and M.C.; Supervision, M.D. and M.C.; Funding Acquisition, M.D., M.C.P., and M.C.

ACKNOWLEDGMENTS

We thank Leo Valon for designing and making the TIAM_linker_CRY2_IRFP optogenetic plasmid. We thank Fred Etoc for the initial mEOS2-Rac1 construction and for preliminary experiments. M.C. acknowledges financial support from French National Research Agency (LICOP grant ANR-12-JSV5-0002-01). M.C. and M.D. acknowledge funding from French National Research Agency (ANR) Paris-Science-Lettres Program (grant ANR-10-IDEX-0001-02 PSL), Labex CelTisPhyBio (grant ANR-10-LBX-0038), and France-Biomedicine infrastructure supported by ANR grant ANR-10-INSB-04 (Investments for the Future). M.C. and M.C.P. acknowledge INSERM ITMO Plan Cancer 2014–2018 (PC201530).

Received: June 12, 2017

Revised: September 18, 2017

Accepted: October 18, 2017

Published: November 14, 2017

REFERENCES

- Azioune, A., Storch, M., Bornens, M., Théry, M., and Piel, M. (2009). Simple and rapid process for single cell micro-patterning. *Lab Chip* 9, 1640–1642.
- Bement, W.M., Miller, A.L., and von Dassow, G. (2006). Rho GTPase activity zones and transient contractile arrays. *BioEssays* 28, 983–993.
- Bieling, P., Li, T.D., Weichsel, J., McGorty, R., Jreij, P., Huang, B., Fletcher, D.A., and Mullins, R.D. (2016). Force feedback controls motor activity and mechanical properties of self-assembling branched actin networks. *Cell* 164, 115–127.
- Bisi, S., Disanza, A., Malinverno, C., Frittoli, E., Palamidessi, A., and Scita, G. (2013). Membrane and actin dynamics interplay at lamellipodia leading edge. *Curr. Opin. Cell Biol.* 25, 565–573.
- Blažević, O., Mideksa, Y.G., Solman, M., Ligabue, A., Ariotti, N., Nakhaeizadeh, H., Fansa, E.K., Papageorgiou, A.C., Wittinghofer, A., Ahmadian, M.R., and Abankwa, D. (2016). Galectin-1 dimers can scaffold Raf-effectors to increase H-ras nanoclustering. *Sci. Rep.* 6, 24165.
- Bonny, M., Hui, X., Schweizer, J., Kaestner, L., Zeug, A., Kruse, K., and Lipp, P. (2016). C2-domain mediated nano-cluster formation increases calcium signaling efficiency. *Sci. Rep.* 6, 36028.
- Burkel, B.M., Benink, H.A., Vaughan, E.M., von Dassow, G., and Bement, W.M. (2012). A Rho GTPase signal treadmill backs a contractile array. *Dev. Cell* 23, 384–396.
- Castellana, M., Wilson, M.Z., Xu, Y., Joshi, P., Cristea, I.M., Rabinowitz, J.D., Gitai, Z., and Wingreen, N.S. (2014). Enzyme clustering accelerates processing of intermediates through metabolic channeling. *Nat. Biotechnol.* 32, 1011–1018.
- Cebecauer, M., Spitaler, M., Sergé, A., and Magee, A.I. (2010). Signalling complexes and clusters: functional advantages and methodological hurdles. *J. Cell Sci.* 123, 309–320.
- Chazeau, A., Mehidi, A., Nair, D., Gautier, J.J., Leduc, C., Chamma, I., Kage, F., Kechkar, A., Thoumine, O., Rottner, K., et al. (2014). Nanoscale segregation of actin nucleation and elongation factors determines dendritic spine protrusion. *EMBO J.* 33, 2745–2764.
- Das, S., Yin, T., Yang, Q., Zhang, J., Wu, Y.I., and Yu, J. (2015). Single-molecule tracking of small GTPase Rac1 uncovers spatial regulation of membrane translocation and mechanism for polarized signaling. *Proc. Natl. Acad. Sci. U S A* 112, E267–E276.

- Davis, M.J., Ha, B.H., Holman, E.C., Halaban, R., Schlessinger, J., and Boggon, T.J. (2013). RAC1P29S is a spontaneously activating cancer-associated GTPase. *Proc. Natl. Acad. Sci. U S A* *110*, 912–917.
- Duriscic, N., Laparra-Cuervo, L., Sandoval-Álvarez, A., Borbely, J.S., and Lakadamyali, M. (2014). Single-molecule evaluation of fluorescent protein photoactivation efficiency using an in vivo nanotemplate. *Nat. Methods* *11*, 156–162.
- Finkielstein, C.V., Overduin, M., and Capelluto, D.G.S. (2006). Cell migration and signaling specificity is determined by the phosphatidylserine recognition motif of Rac1. *J. Biol. Chem.* *281*, 27317–27326.
- Fricke, F., Beaudouin, J., Eils, R., and Heilemann, M. (2015). One, two or three? Probing the stoichiometry of membrane proteins by single-molecule localization microscopy. *Sci. Rep.* *5*, 14072.
- Fritz, R.D., and Pertz, O. (2016). The dynamics of spatio-temporal Rho GTPase signaling: formation of signaling patterns. *F1000Res* *5*, 749.
- García-Parajo, M.F., Cambi, A., Torreno-Pina, J.A., Thompson, N., and Jacobson, K. (2014). Nanoclustering as a dominant feature of plasma membrane organization. *J. Cell Sci.* *127*, 4995–5005.
- Gautier, J.J., Lomakina, M.E., Bouslama-Oueghlani, L., Derivery, E., Beilinson, H., Faigle, W., Loew, D., Louvard, D., Echard, A., Alexandrova, A.Y., et al. (2011). Clathrin is required for Scar/Wave-mediated lamellipodium formation. *J. Cell Sci.* *124*, 3414–3427.
- Gc, J.B., Gerstman, B.S., Stahelin, R.V., and Chapagain, P.P. (2016). The Ebola virus protein VP40 hexamer enhances the clustering of PI(4,5)P 2 lipids in the plasma membrane. *Phys. Chem. Chem. Phys.* *18*, 7–9.
- Groves, J.T., and Kuriyan, J. (2010). Molecular mechanisms in signal transduction at the membrane. *Nat. Struct. Mol. Biol.* *17*, 659–665.
- Hancock, J.F., and Parton, R.G. (2005). Ras plasma membrane signalling platforms. *Biochem. J.* *389*, 1–11.
- Harding, A.S., and Hancock, J.F. (2008). Using plasma membrane nanoclusters to build better signaling circuits. *Trends Cell Biol.* *18*, 364–371.
- Haugh, J.M., Codazzi, F., Teruel, M., and Meyer, T. (2000). Spatial sensing in fibroblasts mediated by 3' phosphoinositides. *J. Cell Biol.* *151*, 1269–1280.
- Heo, W.D., Inoue, T., Park, W.S., Kim, M.L., Park, B.O., Wandless, T.J., and Meyer, T. (2006). PI(3,4,5)P3 and PI(4,5)P2 lipids target proteins with polybasic clusters to the plasma membrane. *Science* *314*, 1458–1461.
- Hobbs, G.A., Wittinghofer, A., and Der, C.J. (2016). Selective targeting of the KRAS G12C mutant: kicking KRAS when it's down. *Cancer Cell* *29*, 251–253.
- Hodgson, L., Spiering, D., Sabouri-Ghomi, M., Dagliyan, O., DerMardirossian, C., Danuser, G., and Hahn, K.M. (2016). FRET binding antenna reports spatio-temporal dynamics of GDI-Cdc42 GTPase interactions. *Nat. Chem. Biol.* *12*, 802–809.
- Honigsmann, A., van den Bogaart, G., Iraheta, E., Risselada, H.J., Milovanovic, D., Mueller, V., Müller, S., Diederichsen, U., Fasshauer, D., Grubmüller, H., et al. (2013). Phosphatidylinositol 4,5-bisphosphate clusters act as molecular beacons for vesicle recruitment. *Nat. Struct. Mol. Biol.* *20*, 679–686.
- Huang, C.-H., Tang, M., Shi, C., Iglesias, P.A., and Devreotes, P.N. (2013). An excitable signal integrator couples to an idling cytoskeletal oscillator to drive cell migration. *Nat. Cell Biol.* *15*, 1307–1316.
- Iyengar, G., and Rao, M. (2014). A cellular solution to an information-processing problem. *Proc. Natl. Acad. Sci. U S A* *111*, 12402–12407.
- Ji, C., Zhang, Y., Xu, P., Xu, T., and Lou, X. (2015). Nanoscale landscape of phosphoinositides revealed by specific pleckstrin homology (PH) domains using single-molecule superresolution imaging in the plasma membrane. *J. Biol. Chem.* *290*, 26978–26993.
- Johnson, J.L., Erickson, J.W., and Cerione, R.A. (2012). C-terminal di-arginine motif of Cdc42 protein is essential for binding to phosphatidylinositol 4,5-bisphosphate-containing membranes and inducing cellular transformation. *J. Biol. Chem.* *287*, 5764–5774.
- Kennedy, M.J., Hughes, R.M., Peteya, L.A., Schwartz, J.W., Ehlers, M.D., and Tucker, C.L. (2010). Rapid blue-light-mediated induction of protein interactions in living cells. *Nat. Methods* *7*, 973–975.
- Kholodenko, B.N., Hancock, J.F., and Kolch, W. (2010). Signalling ballet in space and time. *Nat. Rev. Mol. Cell Biol.* *11*, 414–426.
- Köster, D.V., Husain, K., Iljazi, E., Bhat, A., Bieling, P., Mullins, R.D., Rao, M., and Mayor, S. (2016). Actomyosin dynamics drive local membrane component organization in an in vitro active composite layer. *Proc. Natl. Acad. Sci. U S A* *113*, E1645–E1654.
- Krause, M., and Gautreau, A. (2014). Steering cell migration: lamellipodium dynamics and the regulation of directional persistence. *Nat. Rev. Mol. Cell Biol.* *15*, 577–590.
- Lawson, C.D., and Burridge, K. (2014). The on-off relationship of Rho and Rac during integrin-mediated adhesion and cell migration. *Small GTPases* *5*, e27958.
- Lebensohn, A.M., and Kirschner, M.W. (2009). Activation of the WAVE complex by coincident signals controls actin assembly. *Mol. Cell* *36*, 512–524.
- Li, L., Shi, X., Guo, X., Li, H., and Xu, C. (2014). Ionic protein-lipid interaction at the plasma membrane: what can the charge do? *Trends Biochem. Sci.* *39*, 130–140.
- Machacek, M., Hodgson, L., Welch, C., Elliott, H., Pertz, O., Nalbant, P., Abell, A., Johnson, G.L., Hahn, K.M., and Danuser, G. (2009). Coordination of Rho GTPase activities during cell protrusion. *Nature* *461*, 99–103.
- Manley, S., Gillette, J.M., Patterson, G.H., Shroff, H., Hess, H.F., Betzig, E., and Lippincott-Schwartz, J. (2008). High-density mapping of single-molecule trajectories with photoactivated localization microscopy. *Nat. Methods* *5*, 155–157.
- Mendoza, M.C., Vilela, M., Juárez, J.E., Blenis, J., and Danuser, G. (2015). ERK reinforces actin polymerization to power persistent edge protrusion during motility. *Sci. Signal.* *8*, ra47.
- Moshfegh, Y., Bravo-Cordero, J.J., Miskolci, V., Condeelis, J., and Hodgson, L. (2014). A Trio-Rac1-Pak1 signalling axis drives invadopodia disassembly. *Nat. Cell Biol.* *16*, 574–586.
- Navarro-Lérida, I., Sánchez-Perales, S., Calvo, M., Rentero, C., Zheng, Y., Enrich, C., and Del Pozo, M.A. (2012). A palmitoylation switch mechanism regulates Rac1 function and membrane organization. *EMBO J.* *31*, 534–551.
- Normanno, D., Boudarène, L., Dugast-Darzacq, C., Chen, J., Richter, C., Proux, F., Bénichou, O., Voituriez, R., Darzacq, X., and Dahan, M. (2015). Probing the target search of DNA-binding proteins in mammalian cells using TetR as model searcher. *Nat. Commun.* *6*, 7357.
- Oikawa, T., Yamaguchi, H., Itoh, T., Kato, M., Ijuin, T., Yamazaki, D., Suetsugu, S., and Takenawa, T. (2004). PtdIns(3,4,5)P3 binding is necessary for WAVE2-induced formation of lamellipodia. *Nat. Cell Biol.* *6*, 420–426.
- Parrini, M.C., Sadou-Dubourgoux, A., Aoki, K., Kunida, K., Biondini, M., Hatzoglou, A., Pouillet, P., Formstecher, E., Yeaman, C., Matsuda, M., et al. (2011). SH3BP1, an exocyst-associated RhoGAP, inactivates Rac1 at the front to drive cell motility. *Mol. Cell* *42*, 650–661.
- Peng, G.E., Wilson, S.R., and Weiner, O.D. (2011). A pharmacological cocktail for arresting actin dynamics in living cells. *Mol. Biol. Cell* *22*, 3986–3994.
- Pertz, O. (2010). Spatio-temporal Rho GTPase signaling—where are we now? *J. Cell Sci.* *123*, 1841–1850.
- Petrie, R.J., Doyle, A.D., and Yamada, K.M. (2009). Random versus directionally persistent cell migration. *Nat. Rev. Mol. Cell Biol.* *10*, 538–549.
- Pezzarossa, A., Zosel, F., and Schmidt, T. (2015). Visualization of HRas domains in the plasma membrane of fibroblasts. *Biophys. J.* *108*, 1870–1877.
- Picas, L., Gaits-Iacovoni, F., and Goud, B. (2016). The emerging role of phosphoinositide clustering in intracellular trafficking and signal transduction. *F1000Res* *5*, 422.
- Plowman, S.J., Muncke, C., Parton, R.G., and Hancock, J.F. (2005). H-ras, K-ras, and inner plasma membrane raft proteins operate in nanoclusters with differential dependence on the actin cytoskeleton. *Proc. Natl. Acad. Sci. U S A* *102*, 15500–15505.
- Raghupathy, R., Anilkumar, A.A., Polley, A., Singh, P.P., Yadav, M., Johnson, C., Suryawanshi, S., Saikam, V., Sawant, S.D., Panda, A., et al. (2015).

- Transbilayer lipid interactions mediate nanoclustering of lipid-anchored proteins. *Cell* 161, 581–594.
- Roob, E., 3rd, Trendel, N., Rein Ten Wolde, P., and Mugler, A. (2016). Cooperative clustering digitizes biochemical signaling and enhances its fidelity. *Biophys. J.* 110, 1661–1669.
- Rossier, O., Ochteau, V., Sibarita, J.B., Leduc, C., Tessier, B., Nair, D., Gatterdam, V., Destaing, O., Albigès-Rizo, C., Tampé, R., et al. (2012). Integrins $\beta 1$ and $\beta 3$ exhibit distinct dynamic nanoscale organizations inside focal adhesions. *Nat. Cell Biol.* 14, 1057–1067.
- Salamon, R.S., and Backer, J.M. (2013). Phosphatidylinositol-3,4,5-trisphosphate: tool of choice for class I PI 3-kinases. *BioEssays* 35, 602–611.
- Schütz, G.J., Schindler, H., and Schmidt, T. (1997). Single-molecule microscopy on model membranes reveals anomalous diffusion. *Biophys. J.* 73, 1073–1080.
- Schwartz, M.A. (1997). Integrins, oncogenes, and anchorage independence. *J. Cell Biol.* 139, 575–578.
- Shibata, A.C.E., Chen, L.H., Nagai, R., Ishidate, F., Chadda, R., Miwa, Y., Naruse, K., Shirai, Y.M., Fujiwara, T.K., and Kusumi, A. (2013). Rac1 recruitment to the archipelago structure of the focal adhesion through the fluid membrane as revealed by single-molecule analysis. *Cytoskeleton (Hoboken)* 70, 161–177.
- Shivanandan, A., Unnikrishnan, J., and Radenovic, A. (2015). On characterizing membrane protein clusters with model-free spatial correlation approaches. *bioRxiv*. <https://doi.org/10.1101/030718>.
- Specht, C.G., Grünewald, N., Pascual, O., Rostgaard, N., Schwarz, G., and Triller, A. (2011). Regulation of glycine receptor diffusion properties and gephyrin interactions by protein kinase C. *EMBO J.* 30, 3842–3853.
- Stahelin, R.V., Scott, J.L., and Frick, C.T. (2014). Cellular and molecular interactions of phosphoinositides and peripheral proteins. *Chem. Phys. Lipids* 182, 3–18.
- Théry, M., Racine, V., Piel, M., Pépin, A., Dimitrov, A., Chen, Y., Sibarita, J.B., and Bornens, M. (2006). Anisotropy of cell adhesive microenvironment governs cell internal organization and orientation of polarity. *Proc. Natl. Acad. Sci. U S A* 103, 19771–19776.
- Tian, T., Harding, A., Inder, K., Plowman, S., Parton, R.G., and Hancock, J.F. (2007). Plasma membrane nanoswitches generate high-fidelity Ras signal transduction. *Nat. Cell Biol.* 9, 905–914.
- Tran, T.N., Drab, K., and Daszykowski, M. (2013). Revised DBSCAN algorithm to cluster data with dense adjacent clusters. *Chemometr. Intell. Lab. Syst.* 120, 92–96.
- Um, K., Niu, S., Duman, J.G., Cheng, J.X., Tu, Y.K., Schwechter, B., Liu, F., Hiles, L., Narayanan, A.S., Ash, R.T., et al. (2014). Dynamic control of excitatory synapse development by a Rac1 GEF/GAP regulatory complex. *Dev. Cell* 29, 701–715.
- Valon, L., Etoc, F., Remorino, A., di Pietro, F., Morin, X., Dahan, M., and Coppey, M. (2015). Predictive spatiotemporal manipulation of signaling perturbations using optogenetics. *Biophys. J.* 109, 1785–1797.
- van den Bogaart, G., Meyenberg, K., Risselada, H.J., Amin, H., Willig, K.I., Hubrich, B.E., Dier, M., Hell, S.W., Grubmüller, H., Diederichsen, U., and Jahn, R. (2011). Membrane protein sequestering by ionic protein-lipid interactions. *Nature* 479, 552–555.
- Veatch, S.L., Machta, B.B., Shelby, S.A., Chiang, E.N., Holowka, D.A., and Baird, B.A. (2012). Correlation functions quantify super-resolution images and estimate apparent clustering due to over-counting. *PLoS ONE* 7, e31457.
- Viaud, J., Lagarrigue, F., Ramel, D., Allart, S., Chicanne, G., Ceccato, L., Courilleau, D., Xuereb, J.M., Pertz, O., Payrastra, B., and Gaits-Iacovoni, F. (2014). Phosphatidylinositol 5-phosphate regulates invasion through binding and activation of Tiam1. *Nat. Commun.* 5, 4080.
- Wang, J., and Richards, D.A. (2012). Segregation of PIP2 and PIP3 into distinct nanoscale regions within the plasma membrane. *Biol. Open* 1, 857–862.
- Wang, S., Watanabe, T., Matsuzawa, K., Katsumi, A., Kakeno, M., Matsui, T., Ye, F., Sato, K., Murase, K., Sugiyama, I., et al. (2012). Tiam1 interaction with the PAR complex promotes talin-mediated Rac1 activation during polarized cell migration. *J. Cell Biol.* 199, 331–345.
- Weiger, M.C., Wang, C.C., Krajcovic, M., Melvin, A.T., Rhoden, J.J., and Haugh, J.M. (2009). Spontaneous phosphoinositide 3-kinase signaling dynamics drive spreading and random migration of fibroblasts. *J. Cell Sci.* 122, 313–323.
- Wertheimer, E., Gutierrez-Uzquiza, A., Roseblit, C., Lopez-Haber, C., Sosa, M.S., and Kazanietz, M.G. (2012). Rac signaling in breast cancer: a tale of GEFs and GAPs. *Cell. Signal.* 24, 353–362.
- Wittinghofer, A., ed. (2014). *Ras Superfamily Small G Proteins: Biology and Mechanisms 1* (Springer). <https://doi.org/10.1007/978-3-7091-1806-1>. <http://www.springer.com/us/book/9783709118054>.
- Woods, B., Kuo, C.C., Wu, C.F., Zyla, T.R., and Lew, D.J. (2015). Polarity establishment requires localized activation of Cdc42. *J. Cell Biol.* 211, 19–26.
- Yang, H.W., Collins, S., and Meyer, T. (2016). Locally excitable Cdc42 signals steer cells during chemotaxis. *Nat. Cell Biol.* 18, 191–201.
- Zhang, B., Gao, Y., Moon, S.Y., Zhang, Y., and Zheng, Y. (2001). Oligomerization of Rac1 gtpase mediated by the carboxyl-terminal polybasic domain. *J. Biol. Chem.* 276, 8958–8967.
- Zhou, Y., and Hancock, J.F. (2015). Ras nanoclusters: versatile lipid-based signaling platforms. *Biochim. Biophys. Acta Mol. Cell Res.* 1853, 841–849.

ARTICLE

DOI: 10.1038/s41467-018-07286-8

OPEN

Optogenetic dissection of Rac1 and Cdc42 gradient shaping

S. de Beco¹, K. Vaidžiulytė¹, J. Manzi¹, F. Dalier², F. di Federico¹, G. Cornilleau¹, M. Dahan¹ & M. Coppey¹

During cell migration, Rho GTPases spontaneously form spatial gradients that define the front and back of cells. At the front, active Cdc42 forms a steep gradient whereas active Rac1 forms a more extended pattern peaking a few microns away. What are the mechanisms shaping these gradients, and what is the functional role of the shape of these gradients? Here we report, using a combination of optogenetics and micropatterning, that Cdc42 and Rac1 gradients are set by spatial patterns of activators and deactivators and not directly by transport mechanisms. Cdc42 simply follows the distribution of Guanine nucleotide Exchange Factors, whereas Rac1 shaping requires the activity of a GTPase-Activating Protein, β 2-chimaerin, which is sharply localized at the tip of the cell through feedbacks from Cdc42 and Rac1. Functionally, the spatial extent of Rho GTPases gradients governs cell migration, a sharp Cdc42 gradient maximizes directionality while an extended Rac1 gradient controls the speed.

¹Laboratoire Physico Chimie Curie, Institut Curie, PSL Research University, Sorbonne Université, CNRS, 75005 Paris, France. ²PASTEUR, Département de chimie, École normale supérieure, CNRS UMR 8640, PSL Research University, Sorbonne Université, 75005 Paris, France. Correspondence and requests for materials should be addressed to M.C. (email: mathieu.coppey@curie.fr)

Cell migration plays a major role in various biological functions, including embryonic development, immune response, wound closure, and cancer invasion. Cells, either isolated or in cohesive groups, are able to respond to many types of spatially distributed environmental cues, including gradients of chemoattractants^{1,2}, of tissue stiffness (durotaxis)^{3–5}, and of adhesion (haptotaxis)^{6,7}. To sense and orient their migration accordingly, cells need to integrate complex and noisy signals and to polarize along the selected direction. A simple explanation for such directed migration would be to consider that external gradients are directly translated into internal gradients. However, recent works^{8–10} point to a two-tiered mechanism. First, a set of signaling proteins (Rho GTPases and Ras) behave as an excitable system that spontaneously establish intracellular membrane-bound gradients, conferring the ability of cells to polarize even in the absence of external stimuli. Second, a sensing machinery based on membrane receptors aligns the polarization axis along the direction of external gradient cues. In the present work, we address the mechanisms shaping the Rho GTPases gradients at the front of randomly migrating cells.

Rho GTPases are known to play a key role in orchestrating the spatially segregated activities that define the polarity axis of migrating cells. At the cell front, membrane protrusions fueled by actin polymerization push the cell forward, while retraction of the cell back depends on acto-myosin contractility^{11–13}. The schematic view is that front-to-back gradients of Cdc42 and Rac1 define the cellular front, while RhoA is mostly active at the back. Cdc42 is known to be required for filopodia formation, through N-WASP-mediated activation of the ARP2/3 complex as well as F-actin bundling proteins such as fascin and formin^{11,14}. Conversely, Rac1 is involved in branched actin polymerization and lamellipodia formation, through WAVE-mediated activation of the ARP2/3 complex¹⁵. RhoA is responsible for stress fiber formation and retraction of the cellular tail through Rho kinase-mediated contraction of myosin II^{16,17}. In reality the situation is more complex since RhoA is also active at the very front of migrating mouse embryonic fibroblasts^{18, 19} and is involved in actin polymerization through Diaphanous-related formins as well as focal adhesions^{20,21}. In addition, the Rho GTPase family contains more than the three members aforementioned, with more than 20 proteins having been discovered^{20,22}. Despite the fact that these other members are classified in the three Cdc42, Rac1, and RhoA sub-families, they present overlapping activities.

Three main classes of proteins regulate the activity of Rho GTPases. Guanine Exchange Factors (GEFs) activate Rho GTPases by promoting the exchange from GDP to GTP, whereas GTPase-activating proteins (GAPs) inhibit Rho GTPases by catalyzing the hydrolysis of GTP²³. A multitude of GEFs and GAPs ensure signaling specificity and fine-tuned regulation. In addition, guanine-nucleotide dissociation inhibitors (GDIs) are negative regulators of Rho GTPases, extracting them from the plasma membrane and blocking their interactions with GEFs^{24,25}. GEFs and GAPs can be localized and activated by upstream factors such as receptor tyrosine kinases or interaction with lipids such as PIP₃^{26,27}, hereby connecting the polarization machinery with the sensing one. Moreover, complex crosstalks connect Rho GTPases and their interactors, resulting in a signaling network that finely regulates Rho GTPases activities. Although many molecular interactions defining this signaling network have been characterized, we currently have little insight on how these interactions are orchestrated in space to shape Rho GTPase activity patterns.

Positive feedbacks acting on Rac1, Cdc42, and RhoA have been proposed to account for their ability to form gradients spontaneously. Rho GTPase activity pulses would be generated thanks to an excitable system⁹ and specific activators like GEFs would

orient and stabilize them^{8,28}. Yet, activity patterns governed by excitable systems have a propensity to propagate through the whole cell, and inhibitory mechanisms are required to limit their expansion^{29–31}. Three mechanisms could confine Rho GTPase activities. First, Rho GTPase cycles can be locally regulated by GEF and GAP concentrations, whose distributions along the cell would shape Rho GTPase intracellular gradients^{31–34}. Second, anchoring or trapping in the cortical acto-myosin network can decrease diffusion considerably. Since Rho GTPases trigger actin polymerization and branching, this mechanism could act as a negative feedback restricting their activity zones. Third, Rho GTPase extraction from the plasma membrane by GDIs can be locally regulated²⁵, such that deactivation regions could be set by the activity of GDIs. It is unclear which of these mechanisms is responsible for the formation of Rho GTPase intracellular spatial patterns.

In this work, we show that Cdc42 and Rac1 gradients are formed thanks to a combination of distributed GEFs and GAPs and not directly by diffusion or actin retrograde flow from a localized source. A combination of experimental approaches and minimal mathematical model suggests that: (i) the amount of active Cdc42 simply follows its GEFs distribution thanks to a uniform GAP activity, (ii) the Rac1 gradient requires an additional inhibition at the front by the β 2-chimaerin GAP that shifts its peak of activity and hereby increases its spatial extent. We show that the localized activity of β 2-chimaerin depends on both Cdc42 and Rac1, forming a negative feedback on Rac1, and that the actin retrograde flow is required for β 2-chimaerin enrichment. Finally, we show that the resulting spatial properties of Cdc42 and Rac1 gradients govern the directionality and the speed of cell movement, respectively.

Results

Cdc42 and Rac1 gradients show two distinct shapes at the front of migrating cells. We investigated the spatial activity gradients of Cdc42 and Rac1 Rho GTPases at the basal plasma membrane by imaging FRET biosensors based on an intramolecular fusion between Rac1 and a PAK1 binding domain³⁵. HeLa cells stably expressing FRET reporters were left to migrate randomly on glass coverslips, and were imaged using total internal reflection fluorescence (TIRF) microscopy. The FRET ratio was calculated as a proxy for GTPase activity. Front-to-back gradients of either Cdc42 or Rac1 activity were measured from the cell protruding edge to the nucleus (Fig. 1a). As previously reported in neutrophils⁹, we observed gradients that differed both in shape and in spatial extent. Cdc42 gradient was steep and monotonous, peaking at the protruding edge, and presenting an exponentially decaying profile of characteristic length $d = 8.3 \mu\text{m} \pm 0.6 \mu\text{m}$ (SEM, $n = 19$). In contrast, Rac1 gradient peaked at a distance $d = 5.8 \pm 0.5 \mu\text{m}$ from the cell edge, and then decayed with a characteristic length $d = 9.6 \mu\text{m} \pm 0.7 \mu\text{m}$ (characteristic length of the exponentially decaying part, $n = 31$). We defined the extent of the gradient by the distance between the tip of the cell and the point where the signal reaches half-amplitude. The extent for Rac1 was $d = 14.6 \pm 0.7 \mu\text{m}$, compared to $d = 8.9 \pm 0.6 \mu\text{m}$ for Cdc42 (Fig. 1b). Interestingly, these observations match those reported for gradients in other cell lines^{9,36}. We thus questioned what could be the mechanisms generating these gradients and accounting for their distinct shapes.

Two generic classes of models can account for the patterning of spatially graded distributions²⁹. The first class relies on transport mechanisms (diffusion, flow) to establish gradients from a localized source (Fig. 1c, d). A canonical example is the synthesis–diffusion–degradation model, which has been heavily discussed in the context of the Bicoid morphogen gradient³⁷. The

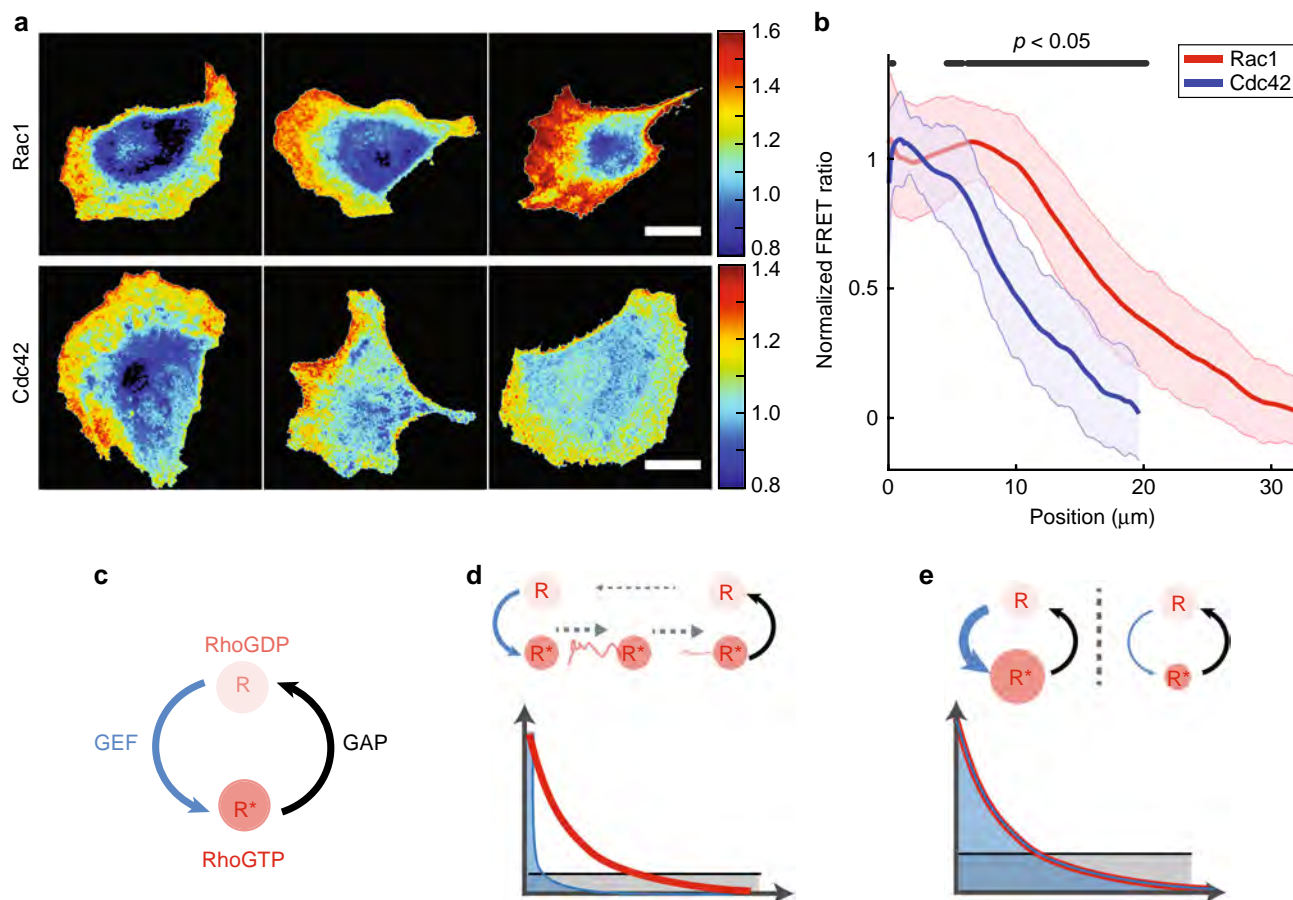


Fig. 1 Rac1 and Cdc42 activity gradients have different shapes. **a** FRET biosensors were used to monitor Rac1 (top) or Cdc42 (bottom) activity in freely migrating HeLa cells. GTPase activity is measured by the FRET ratio, and represented with a color scale. Several representative cells are shown. Scale bar: 20 μm . **b** Mean normalized FRET ratio of Rac1 (red) and Cdc42 (blue) is plotted as a function of the distance from the cell edge. The error bars indicate the standard deviation (s.d.) of $n = 31$ (Rac1) or $n = 19$ (Cdc42) cells. Black segments at the top show positions at which the curves are statistically different ($p < 0.05$, Wilcoxon's rank sum test). **c** Rho GTPase cycle, where the protein switches between an inactive and active state thanks to activators (GEFs) and deactivators (GAPs). **d, e** Two simplified mechanisms can explain the formation of cellular-scale Rho GTPase gradients. **d** A sharply localized GEF (blue profile) acts as a punctual source of active Rho GTPases (red) that are further transported by diffusion or flow (dashed gray arrows) until they reverse to the inactive state thanks to a GAP (black). **e** A cellular-scale distributed GEF locally activates the Rho GTPase such that both have the same profile

second class of models assumes a graded distribution of activators and deactivators (Fig. 1c, e). In this context, the local concentration is set by the local balance between activation and deactivation. This second class of model has also been proposed to explain the establishment of morphogen gradients, e.g. for the formation of the bone morphogenetic protein gradient that patterns the dorso-ventral axis of the early *Xenopus* embryo^{38,39}.

Cdc42 and Rac1 gradients are shaped by spatially distributed GEFs and GAPs but not by diffusion. In order to distinguish between these two classes of models, we opted for an input–output relationship approach. We used optogenetics^{40,41} to impose activation gradients of either Intersectin-1 (ITSN) or T-Cell Lymphoma Invasion and Metastasis 1 (TIAM1), two GEFs specifically activating Cdc42 or Rac1, respectively. We used fusions of CRY2 with the DHPH catalytic domain of ITSN or TIAM to activate specifically Cdc42 or Rac1⁴¹ (Fig. 2c). A home-made illumination setup using a DMD (Digital Micromirror Device⁴²) allowed us to shine spatial gradients of light with an 8-bit gray level resolution. Cells were confined on round micro-patterns to prevent cell shape polarity⁴³ and gradients of light with slopes ranging from 1 \times to 4 \times were applied (Fig. 2a). As we could predict in a previous work⁴⁴, recruitment of the

cytoplasmic optogenetic partner CRY2 to the basal plasma membrane followed the stimulation signal with the addition of an exponential decaying tail of 5 μm characteristic length due to the diffusion of CIBN-CRY2 dimers at the membrane (Fig. 2b). This allowed us to tune precisely the spatial distribution of desired GEFs and test the relationship between the activation input and the output in terms of GTPase activity. If any transport mechanism (model 1) was taking place, we would expect a difference in the spatial distribution of the output compared to the input. For example, diffusion would give rise to a more extended distribution of the output by the addition of a length scale $\ell_{\text{diff}} = \sqrt{\tau D}$, where τ is the lifetime of the Rho GTPase in its active GTP-bound state and D is its lateral diffusion coefficient. Contrarily, model 2 predicts that the spatial distribution of the output would mirror the distribution of the input, given that deactivators are uniform. Indeed, we reasoned that the optogenetic activation would dominate the other sources of activation such that the input–output relationship would reveal the distribution of the deactivators.

To determine whether Cdc42 and Rac1 followed the imposed activation pattern, we used downstream effectors as reporters of GTPase activity. The protein PAK1 is activated downstream of both Cdc42 and Rac1. We monitored the basal membrane recruitment of a PAK1-iRFP fluorescent reporter following

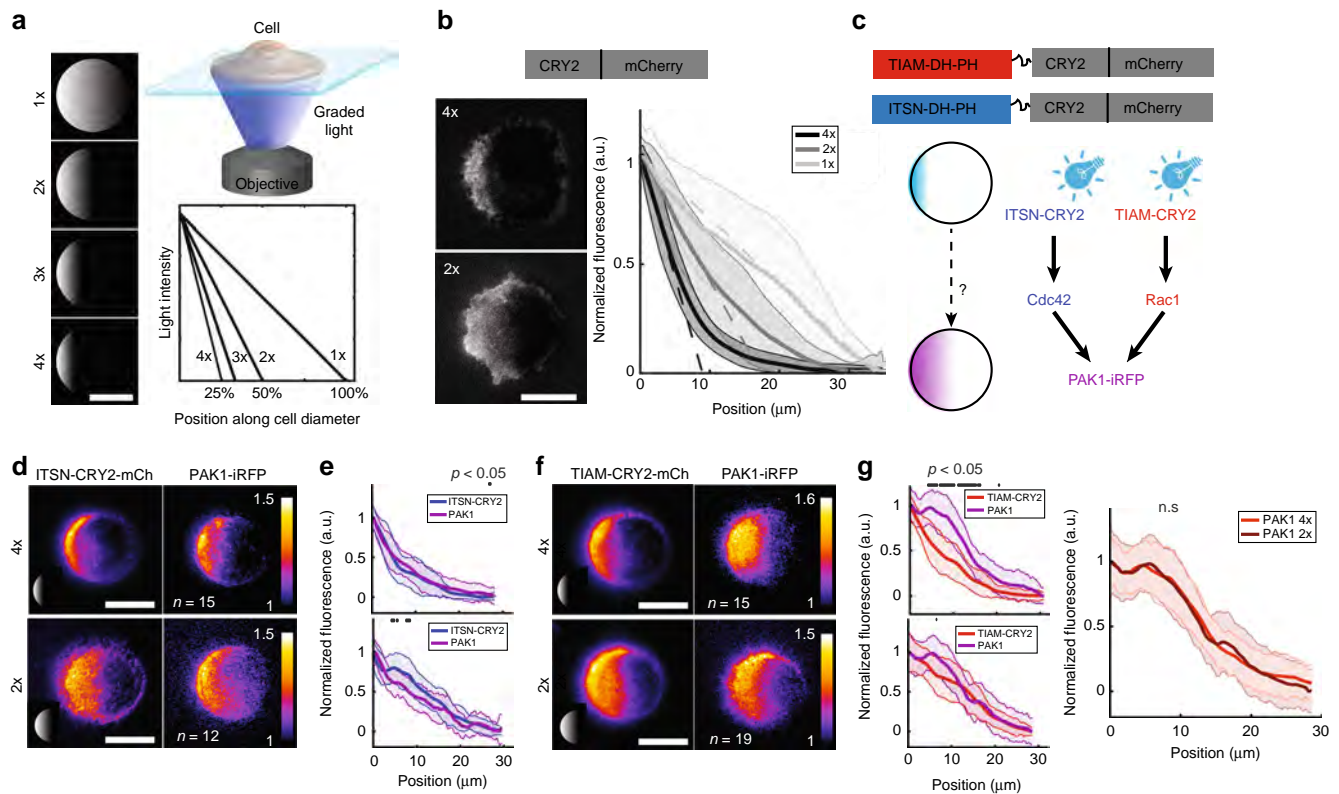


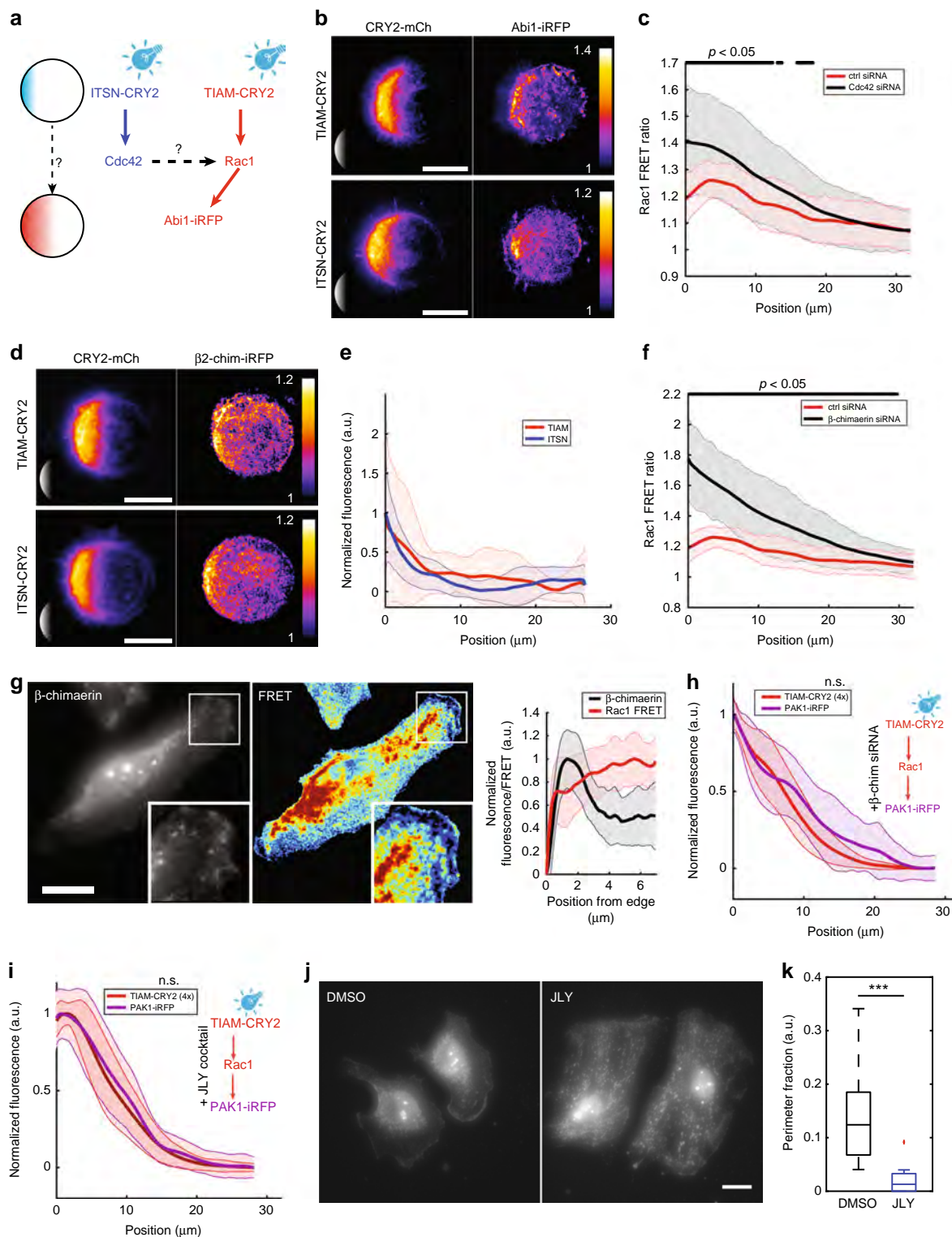
Fig. 2 Cdc42 and Rac1 have different responses to GEF activation. **a** We imposed GEF activity gradients of different slopes using optogenetics. Patterned illumination with grayscale levels (left) was shone onto the samples, imposing linear light gradients of the same amplitude but different spatial extents on cells attached on round micropatterns of 35 μm in diameter (top right). The reference gradient called 1 \times spans over the whole diameter of the cell. The gradient 2 \times spans over a half cell diameter, and therefore has a slope twice as sharp as for the gradient 1 \times (bottom right). **b** Membrane recruitment of the optogenetic partner CRY2-mCherry to the basal side of cells on round micro-patterns following 30 min of illumination with 4 \times (top left) and 2 \times (bottom left) gradients. mCherry fluorescence (solid lines) was measured along the cell diameter following illumination with 1 \times (light gray), 2 \times (medium gray) and 4 \times (black) gradients (dashed lines). Error bars indicate the s.d. of $n = 15$ (1 \times), $n = 24$ (2 \times) and $n = 15$ (4 \times) cells. **c** We activated GEFs of Cdc42 (ITSN) or Rac1 (TIAM) with light gradients and measured the fluorescence pattern of PAK1-iRFP. Schemes at the top represent the fusion proteins used. **d** PAK1-iRFP recruitment following 4 \times (top) or 2 \times (bottom) activation gradients of ITSN. Fluorescence was recorded using TIRFM in HeLa cells on round micro-patterns, and initial fluorescence was subtracted for normalization. Micrographs represent the averaged fluorescence of $n = 15$ (4 \times , top) or $n = 12$ (2 \times , bottom) cells. Insets show the illumination patterns (not to scale). **e** Normalized fluorescence of ITSN-CRY2-mCherry (blue) and PAK1-iRFP (purple) was measured along the cell diameter and averaged (solid lines). Error bars: s.d. Gray lines at the top show positions at which the curves are statistically different ($p < 0.05$, Wilcoxon's rank sum test). **f** PAK1-iRFP recruitment following 4 \times (top, $n = 15$) or 2 \times (bottom, $n = 19$) activation gradients of TIAM. **g** Normalized fluorescence of TIAM-CRY2-mCherry (red) and PAK1-iRFP (purple) along the cell diameter of $n = 15$ (4 \times , top) or $n = 19$ (2 \times , bottom) cells, Error bars: s.d. Gray: Wilcoxon's rank sum test ($p < 0.05$). Single cell data for **e** and **g** are presented in Supplementary Figure 3. Scale bars: 20 μm

gradient activation of each one of the GTPases (Fig. 2c). As controls, we verified that the observed recruitment of PAK1-iRFP was not due to fluorescence bleed-through or nonspecific activity of CRY2-mCherry (Supplementary Figure 1a), nor to volume effects or cell deformation (Supplementary Figure 1b). Importantly, we also verified that the GEF DHPH domains used in our optogenetic approach were truly specific (Supplementary Figure 2). PAK1-iRFP recruitment patterns followed the activation gradients of ITSN-CRY2 remarkably well, independently of their spatial extents (Fig. 2d, e, Supplementary Movie 1). We could not detect any significant difference between the PAK1 response and the activating ITSN gradients, independently of their spatial extents (Fig. 2d, e, Supplementary Movie 1), up to the resolution of our measurement estimated as $\sim 2 \mu\text{m}$ (two standard deviations of the spatial extent). This result suggests that GEF activity levels are sufficient to shape Cdc42 activity patterns without the requirement of other mechanisms. Conversely, PAK1-iRFP spatial recruitment was independent of the shape of the activating TIAM-CRY2 gradient. It did not follow the sharpest activation gradient (4 \times), and the peak at 6 μm from the protrusion edge was

present from the beginning of the stimulation (Supplementary Figure 4, Supplementary Movie 2) despite its absence from the gradients of TIAM-CRY2 (Fig. 2f, g). Interestingly, the PAK1-iRFP gradient obtained with our synthetic approach matched the Rac1 gradient observed in native cells (Fig. 1b). We thus sought to discriminate between two possibilities explaining how the Rac1 gradient is shaped: whether shaping involves transport or nonuniformly distributed deactivators.

A crosstalk between Cdc42 and Rac1 through GEFs and GAPs contributes to Rac1 gradient shaping.

A complex crosstalk between the Cdc42 and Rac1 pathways has been shown previously^{12,45}. We questioned whether such network could explain the complex pattern of Rac1 activity we observed. We used the Abi1-iRFP fusion protein as a reporter of Rac1 activity. Abi1 is part of the WAVE complex that has been shown to be activated specifically by Rac1 but not by Cdc42⁴⁶ (Fig. 3a). We observed that Abi1 is activated at the cell edge following TIAM but also ITSN optogenetic activation (Fig. 3b), suggesting that Cdc42 directly or indirectly activates Rac1. Interestingly, in both



cases the induced Abi1 recruitment was more restricted to the cell border than the activating gradients (Supplementary Figure 5). This observation is in accordance with the known distribution of the WAVE complex at the tip of the lamellipodia⁴⁷, suggesting a compartmentalization independent of the immediate Rho GTPase activation. Yet, in addition to the positive crosstalk, we also observed a cross inactivation of Rac1 by Cdc42. When we inhibited Cdc42 by siRNA (Supplementary Figure 6a), we observed an increase of Rac1 activity at the cell front as measured by the non-normalized FRET profile (Fig. 3c). Strikingly, the

bump of Rac1 activity 6 μm from the cell edge was abolished in this condition. Since the overall effect of Cdc42 depletion is to increase Rac1 activity, we reasoned that the dominant role of Cdc42 on Rac1 is to specifically activate a GAP inhibiting Rac1.

β2-chimaerin is a GAP of Rac1 that was shown to be activated at the protrusion edge downstream of chemotactic signals⁴⁸. We monitored the recruitment of the β2-chimaerin-iRFP reporter following the optogenetic activation of TIAM or ITSN. We could observe that both pathways could recruit β2-chimaerin at the cell edge, in a very localized fashion similar to the WAVE recruitment

Fig. 3 Cdc42 and β 2-chimaerin are involved in shaping the activity gradient of Rac1. **a** We activated GEFs of Cdc42 (ITSN) or Rac1 (TIAM) with light gradients and measured the fluorescence pattern of Abi1-iRFP. **b** Averaged Abi1-iRFP recruitment (right column) following 4 \times activation gradients (left column) of TIAM ($n = 10$, top) or ITSN ($n = 11$, bottom) visualized using TIRFM on round micro-patterns. The averaging procedure is explained in the Methods section. Insets show the illumination patterns (not to scale). **c** Non-normalized Rac1 FRET ratio profiles along cell diameters of cells treated with control siRNA ($n = 38$, red) or Cdc42-directed siRNA ($n = 37$, black). Error bars: s.d. Gray lines at the top show positions at which the curves are statistically different ($p < 0.05$, Wilcoxon's rank sum test). **d, e** β 2-chimaerin-iRFP (right) recruitment following 4 \times activation gradients (left) of TIAM ($n = 11$, top) or ITSN ($n = 12$, bottom), imaged in TIRFM on round micro-patterns. **d** Micrographs represent the averaged fluorescence (see Methods). **e** Normalized fluorescence of β 2-chimaerin-iRFP was measured along the cell diameter following the activation of ITSN-CRY2-mCherry (blue, $n = 12$) or TIAM-CRY2-mCherry (red, $n = 11$). Error bars: s.d. **f** Non-normalized Rac1 FRET ratio profiles along cell diameters of cells treated with control siRNA ($n = 38$, red) or β 2-chimaerin-directed siRNA ($n = 25$, black). Error bars: s.d. Gray: Wilcoxon rank sum test ($p < 0.05$). **g** β 2-chimaerin staining (left, Gamma correction was applied to images in order to visualize the full dynamics) compared to normalized Rac1 FRET (middle) in the same cells. Insets show zoomed regions of the cell edge. Levels of β 2-chimaerin (black) and Rac1 activity (red) are anticorrelated at the cell front (right panel, $n = 8$, Error bars: s.d.). **h** PAK1-iRFP (purple) recruitment following 4 \times activation gradients of TIAM (red) after treatment with β 2-chimaerin-directed siRNA ($n = 14$). Curves were found not significantly different on their whole length (Wilcoxon, $p > 0.05$). **i** PAK1-iRFP (purple) recruitment following 4 \times activation gradients of TIAM (red) after treatment with JLY cocktail ($n = 23$). n.s., nonsignificant. **j** β 2-chimaerin staining after DMSO (left) or JLY cocktail (right) treatment. **k** Fraction of cell perimeter showing β 2-chimaerin signal at the cell edge larger than in the cytosol (DMSO: $n = 11$, JLY: $n = 10$). Fluorescence at the cell edge was measured along a 1- μ m-thick line obtained from the thresholding-based segmentation of the cell shape. The signal in the cytosol was evaluated from a 1 μ m-thick line outlining that cell edge on its cytosolic side. Box plots represent the median, interquartile (box), 1.5 IQR (whiskers), and outliers (red crosses). Statistical significance was evaluated using Wilcoxon's rank sum test. *** $p \leq 0.001$. Scale bars: 20 μ m

(Fig. 3d, e), suggesting that this GAP recruitment is conditioned by other signaling components belonging to the tip of the lamellipodia, in accordance with the colocalization between β 2-chimaerin and F-actin observed in the lamellipodia of unstimulated cells (Supplementary Figure 7). Accordingly, inhibiting β 2-chimaerin using siRNA (Supplementary Figure 6b) led to a strong increase of Rac1 activity especially at the cell front such that the bump was abolished (Fig. 3f). This result suggests that β 2-chimaerin might act downstream of Cdc42 and Rac1 to inhibit Rac1 locally at the cell front. Indeed, at the front of randomly migrating cells we observed an anticorrelation between β 2-chimaerin and Rac1 activities measured by FRET (Fig. 3g). We could verify that the observed localization of β 2-chimaerin at the cell edge was not due to volume effects related to the local membrane ruffling activity (Supplementary Figure 8). We further confirmed the direct role of β 2-chimaerin in shaping the Rac1 gradient by inducing the sharp Rac1 activation (4 \times) using optogenetics in β 2-chimaerin-depleted cells, which resulted in a PAK1 gradient that now matched the activating profile (Fig. 3h).

Orthogonally to the previous experiments, we also tested the role of transport in shaping the Rac1 gradient. Given that we observed the same PAK1 spatial profile for two distinct TIAM-CRY2 activating gradients (Fig. 2g), we excluded diffusion as it would have smoothed both input distributions. Conversely, the retrograde flow of actin in the lamellipodia can give rise to two similar outputs if the distribution of the flow velocities is ultimately limiting the spatial expansion of the gradient. When cells were treated with the Jaspilakinolide-LatrunculinB-Y27632 (JLY) drug cocktail that freezes actin dynamics⁴⁹, we indeed observed a Rac1 activity gradient that matched the sharp (4 \times) TIAM-CRY2 input gradient (Fig. 3i). Surprisingly, this result shows that the actin retrograde flow can also account for the bump observed in the endogenous Rac1 gradient besides our previously found role for β 2-chimaerin. However, this effect could be indirect if the retrograde flow was acting not on Rac1 itself but on the machinery required for proper β 2-chimaerin localized distribution. To test this hypothesis, we compared the distribution of β 2-chimaerin in control and JLY-treated cells (Fig. 3j). β 2-chimaerin localization disappeared from the tip of migrating cells in JLY-treated cells, confirming the indirect role of actin dynamics (Fig. 3k).

A minimal model of local reactions recapitulates Cdc42 and Rac1 gradient shaping. Given the numerous layers of

interactions that we identified experimentally, we sought for a minimal model that would capture the main mechanisms giving rise to the cellular-scale properties of the Cdc42 and Rac1 gradients. To this end, we built a one-dimensional model, where the x -axis spanned across the cell from $x=0$ to $x=35 \mu\text{m}$. We assumed that the Rho GTPases were activated and deactivated with first-order kinetics, and that levels of Rho GTPases equilibrated on a fast time scale. We assumed that the total amount of Rho GTPase R_{tot} was not limiting. Eventually, we excluded diffusion and flow, such that the model was purely local. Thus, the local concentration of active Rho GTPase $R^*(x)$ at steady-state is of the form:

$$\frac{R^*(x)}{R_{\text{tot}}} = \frac{\sum_i \alpha_i [\text{GEF}]_i(x)}{\sum_i \beta_i [\text{GAP}]_i(x)}, \quad (1)$$

where $[\text{GEF}]_i(x)$ and $[\text{GAP}]_i(x)$ are the concentration profiles of GEFs and GAPs, and α_i and β_i their associated effective activation and deactivation rates, which can be a function of the concentration of the Rho GTPases themselves in the case of cross-talks. From the full set of identified interactions (Fig. 4a), we could extract a minimal model explaining the formation of Cdc42 and Rac1 gradients (Fig. 4b). For Cdc42, the shape of the gradient can be simply given by an exponentially distributed GEF and uniform GAP (Fig. 4c):

$$\text{Cdc42}^*(x) \propto \frac{\alpha_C e^{-x/\lambda}}{\beta_C}, \quad (2)$$

where λ is the decay length measured for Cdc42 itself (about 10 μm). Note that in the case of optogenetic activation, the optogenetic term $\alpha_{\text{opto}} e^{-x/\lambda}$ most probably dominates the endogenous GEF activity ($\alpha_{\text{opto}} \gg \alpha_C$) such that the induced gradient follows the activating one. For Rac1, our model contains an exponentially distributed GEF of 10 μm decay length and uniform GAP, similarly to Cdc42, but also a second GAP (β 2-chimaerin) exponentially distributed with its own characteristic length $\gamma = 5 \mu\text{m}$:

$$\text{Rac1}^*(x) \propto \frac{\alpha_R e^{-x/\lambda}}{\beta_R + \beta_b e^{-x/\gamma}}, \quad (3)$$

where β_b is the effective rate constant for β 2-chimaerin GAP activity on Rac1. This expression for Rac1 is sufficient to explain the bump (Fig. 4c), the position of which is determined by the ratio $r = \beta_R/\beta_b$ between the strength of the uniform GAP over the

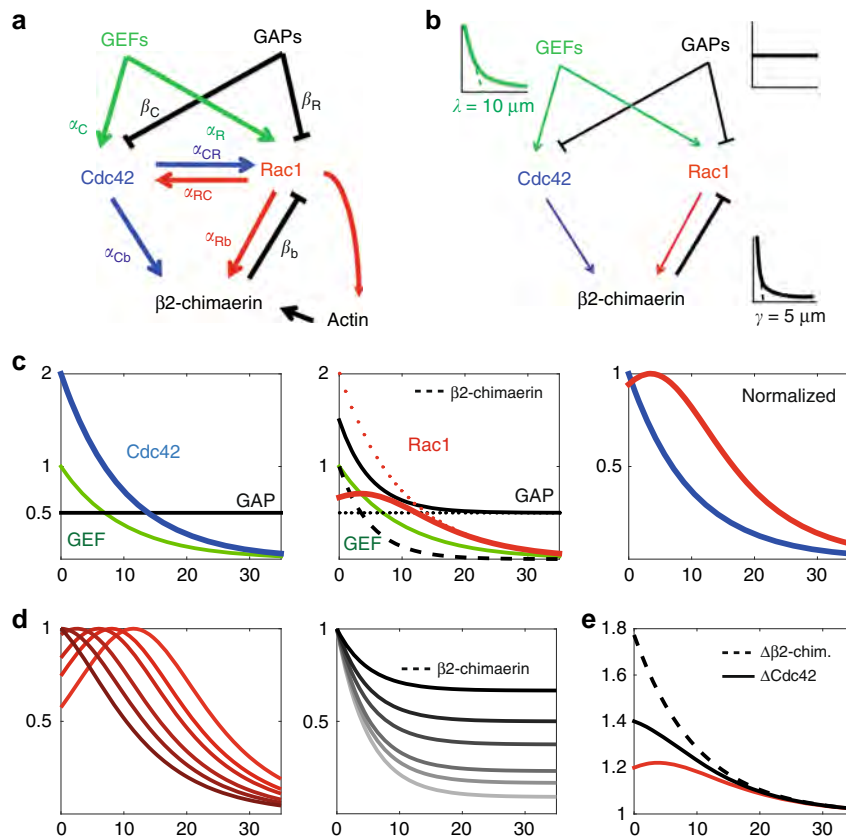


Fig. 4 A minimal model for Cdc42 and Rac1 gradient formation. **a** Full model based on our experimental findings. Activation rates are denoted by α and deactivation rates by β . **b** A minimal model that recapitulates the formation of Cdc42 and Rac1 gradients. **c** Gradient shaping of Cdc42 and Rac1. Since the absolute amplitude of Rho GTPases are unknown, we assigned the following arbitrary values to the rates: $\alpha_C = \alpha_R = 1$; $\beta_C = \beta_R = 0.5$; and $\beta_b = 1$. Left: Cdc42 (blue) is set by an exponentially distributed GEF (green) with a characteristic length $\lambda = 10 \mu\text{m}$ and uniform GAP (black). Middle: Rac1 (red) requires an additional GAP, $\beta 2$ -chimaerin (dashed black, characteristic length $\gamma = 5 \mu\text{m}$), that is localized more sharply at the cell edge than Rac1 GEF (green). The overall GAP activity (plain black) is the sum of $\beta 2$ -chimaerin and a uniform GAP (dashed black). As a result, the putative Rac1 gradient without $\beta 2$ -chimaerin (dashed red) is chopped off at the cell edge resulting in a bell-shaped gradient (plain red). Right: once normalized to 1, Cdc42 and Rac1 gradients present distributions that are similar to the ones measured in cells. **d** Effect of the relative ratio $r = \beta_R / \beta_b$ between uniformly distributed GAPs and the localized gradient of $\beta 2$ -chimaerin on the position of the Rac1 bump. Left: Rac1 gradients obtained with decreasing values of r ($r = 2, 1, 0.6, 0.3, 0.2, 0.1$ respectively from dark to light red). Right: exponentially distributed $\beta 2$ -chimaerin (dashed line) and uniformly distributed GAPs ($\beta_R = 2, 1, 0.6, 0.3, 0.2, 0.1$ from dark to light gray, solid lines) corresponding to the values used for the left plot. **e** Effects of Cdc42 or $\beta 2$ -chimaerin inhibition in silico on the Rac1 gradient ($\alpha_{C_b} = 0.4$, and $\alpha_{R_b} = 0.3$). The profiles are normalized (by the same factor) to match the FRET signal values measured experimentally (Fig. 2c, d)

strength of the localized $\beta 2$ -chimaerin, and by the characteristic lengths of the decaying profiles:

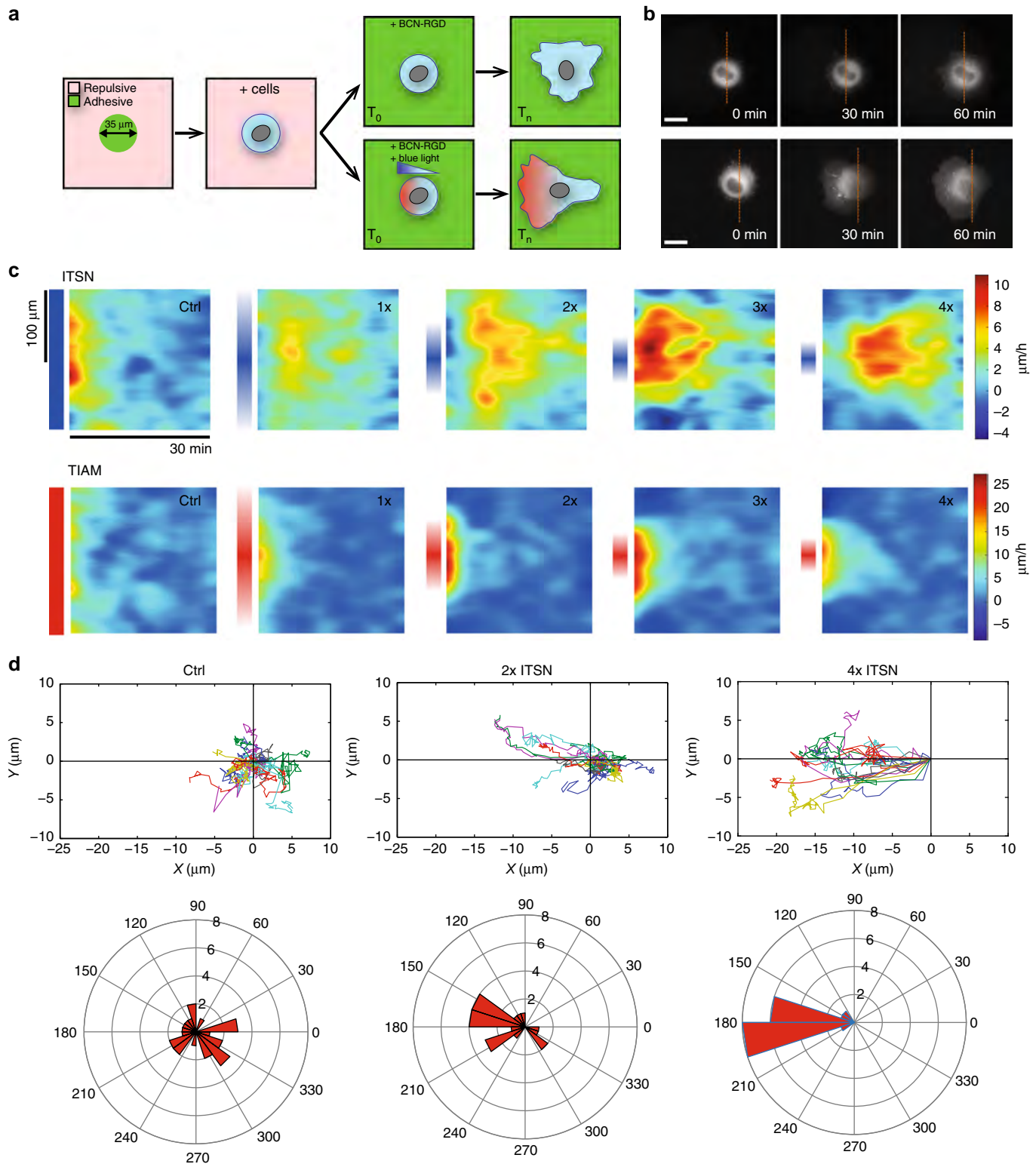
$$x_{\text{bump}} = \gamma \ln \left(\frac{\lambda - \gamma}{r \cdot \gamma} \right). \tag{4}$$

From this relationship, we can see that a bump will be present if $r < (\lambda - \gamma) / \gamma$, which reduces to $r < 1$ using the experimental numbers for the decay lengths, or equivalently $\beta_R < \beta_b$. This means that the strength of the uniform GAP has to be less than the strength of $\beta 2$ -chimaerin to observe a Rac1 bump. The evolution of the bump position as a function of r is presented in Fig. 4d. From the bump position observed in our experiment, we could predict that $\beta 2$ -chimaerin dominates the uniform GAPs by a factor of ~ 2 . This minimal model for Rac1 can be refined to account for the respective roles of Cdc42 and Rac1 in mediating $\beta 2$ -chimaerin activity at the tip (Fig. 4e). Assuming that β_b is a linear function of Cdc42 and Rac1 concentrations: $\beta_b = \beta_{C_b} \text{Cdc42}(x) + \beta_{R_b} \text{Rac1}(x)$, the model shows that Rac1 self-inhibition is required to account for the observed differences in the Rac1 gradient between cells depleted for Cdc42 and cells depleted for $\beta 2$ -chimaerin. Altogether, our minimal modeling approach suggests a simple

mechanism of distributed activators and deactivators that shape Cdc42 and Rac1 gradients such that their spatial extents are ultimately different. We thus anticipated that the spatial extent of these Rho GTPases would play a functional role.

A controlled assay to monitor the dependence of cell migration on Rac1 and Cdc42 gradients.

We next questioned whether the different properties of Cdc42 and Rac1 gradients had an impact on migration properties. For this purpose, we imposed optogenetic gradients of ITSN or TIAM with increasing slopes (Fig. 2a). In order to control the experimental initial conditions, i.e. to prevent initial cell polarity prior to the optogenetic stimulation but still be able to monitor cell movement following it, we opted for a switchable micropatterning technique⁵⁰. Cells were plated on round micropatterns, and would then keep an isometric shape until the surrounding repelling surface was rendered adhesive by coupling a fibronectin-mimicking chemical compound (BCN-RGD) that binds to the modified PLL-PEG repellent (APP). After addition of this reagent, cells were released from patterns and free to migrate on the coverslip (Fig. 5a, b, top row). Optogenetic stimulation with gradients of light concomitantly with the release of adhesion allowed us to study cell migration with one changing



parameter, namely the extent of blue light gradients (Fig. 5a, b, bottom row). From $n \sim 20$ cells per each condition, we quantified the cell edge morphodynamics (see Methods) and averaged them for each activating gradient slope (Fig. 5c). As expected, both Rac1 and Cdc42 biased the membrane protruding activity toward the direction of the gradient. Rac1 led to an immediate cell movement while Cdc42 led to slightly delayed cell movement (Fig. 5c). We observed that cells shifted from an oriented spreading (when the back of the cell kept steady) to a directed

migration (when the back of the cell moved together with the front) by increasing the gradient slope (Supplementary Movies 3, 4). Yet, the center of mass of cells monotonously increases its movement toward the gradient as the gradient slope increased (Fig. 5d) suggesting that the quantitative properties of the gradients have a differential role in migration.

Cdc42 provides directionality while Rac1 provides speed. In order to assess the quantitative effect of gradient on motility, we

Fig. 5 Scheme of the quantitative migration assay. **a** Cells are seeded on 35 μm round patterns. After complete adhesion, the adhesive reagent BCN-RGD is added and binds to the coverslip's surface, allowing free 2D cell migration (top). Directed migration can be triggered by optogenetic activation of GEFs through light gradients at the same time as cell adhesion is released (bottom). **b** Examples of cells expressing CIBN-GFP-CAAX and TIAM-CRY2-mCherry with (3 \times gradient, bottom) or without (top) photo-activation (visualized: TIAM-CRY2-mCherry). Time indicates the duration after addition of BCN-RGD and concomitant blue light illumination. The dashed orange line corresponds to the initial position of the cell center. **c, d** HeLa cells expressing CIBN-GFP-CAAX and ITSN-CRY2-mCherry or CIBN-GFP-CAAX and TIAM-CRY2-mCherry were illuminated with various gradients of light as the adhesive patterns were released. **c** Average morphodynamic maps for each condition (ITSN: top, TIAM: bottom). The vertical axis corresponds to the coordinate along the cell contour (centered on the direction of the light gradient) and the horizontal axis corresponds to time. The local velocity of the edge of the cell membrane is color coded accordingly to the bar on the right side. Gradient extents are schemed on the left side of each map. ITSN: $n=25$ (control with uniform illumination), $n=16$ (1 \times gradient), $n=20$ (2 \times), $n=19$ (3 \times) or $n=16$ (4 \times). TIAM: $n=19$ (ctrl), $n=18$ (1 \times), $n=18$ (2 \times), $n=17$ (3 \times), $n=18$ (4 \times). **d** We tracked the position of the centroid of individual cells. Top: Trajectories of cells stimulated with various gradients of ITSN. Bottom: The angles between the displacement vector (initial to final centroid position) and the stimulation axis for each cell are represented in polar coordinates. Scale bars: 20 μm

focused on two coarse-grained parameters: the maximal instantaneous velocity and the precision of the migration orientation. Sharper gradients of either ITSN or TIAM both increased cellular speed. However, activating Rac1 through TIAM had a stronger effect on speed than activating Cdc42 through ITSN (Fig. 6a), consistent with the known effect of Rac1 as a critical factor for lamellipodium formation¹⁵ (Supplementary Figure 9). In fact, even shallow gradients of TIAM induced an enhanced migration speed. In comparison, only sharp gradients of ITSN (3 \times and 4 \times) induced an increased cellular speed, but even in these conditions speed was lower than for equivalent TIAM gradients. Conversely, ITSN gradients had a stronger effect on orientation precision. While 1 \times to 4 \times TIAM gradients had a similar effect on orientation, increasingly sharp gradients of ITSN induced an increasing precision of migration (Fig. 6b). Indeed, the 4 \times ITSN gradient induced the most oriented response (with a remarkable angular precision), consistent with the known role of Cdc42 as a regulator of directed migration^{51,52}, even though this role seems to be cell dependent⁵³. We show here that directed migration is better achieved with sharp Cdc42 gradients similar to the ones measured endogenously in cells (Cdc42 gradient extent measured in migrating cells $d = 8.9 \pm 0.6 \mu\text{m}$, Fig. 1, 4 \times Cdc42 gradient extent imposed and measured through PAK-iRFP $d = 6.1 \pm 0.9 \mu\text{m}$, Fig. 2). Thus, in our experimental model, Cdc42 provides directionality while Rac1 provides speed of movement. These functions appear to be specific of each GTPase, since inhibition of Rac1 abolishes cell speed but not orientation for Cdc42 activation (Fig. 6c, d). Consequently, crossed activities (speed induction by Cdc42, orientation by Rac1) seem to be due to crosstalks between these Rho GTPases. Along this line, a possible functional role for $\beta 2$ -chimaerin is to spatially segregate Rac1 and Cdc42 activities to avoid competition between their functional roles. Indeed, as seen in supplementary figure 10, $\beta 2$ -chimaerin suppression has no effect on cell speed but leads to a significant reduction in angular precision. This suggests that $\beta 2$ -chimaerin limits Rac1 protrusive activity at the very cell front to allow Cdc42 activity to steer cell migration.

The spatial extent but not the amplitude or slope of the Cdc42 gradient matters for directionality. Since we showed that the shape of Rho GTPase activation gradients directly influence the outcome of cell migration, we thus questioned whether cells are actually sensitive to the slope or to the spatial extent of Rho GTPase activation gradients. In fact, in the previous experiments, both parameters varied concomitantly. It is known that cells can sense and process various extra- and intracellular signaling gradients that can hence influence cell polarity and migration^{54–56}. However, it is not known to which quantitative properties of Rho GTPases intracellular signaling gradients cells are sensitive. Using the experimental setup detailed above, we could independently test the effect of gradient slope or spatial extent. When we applied

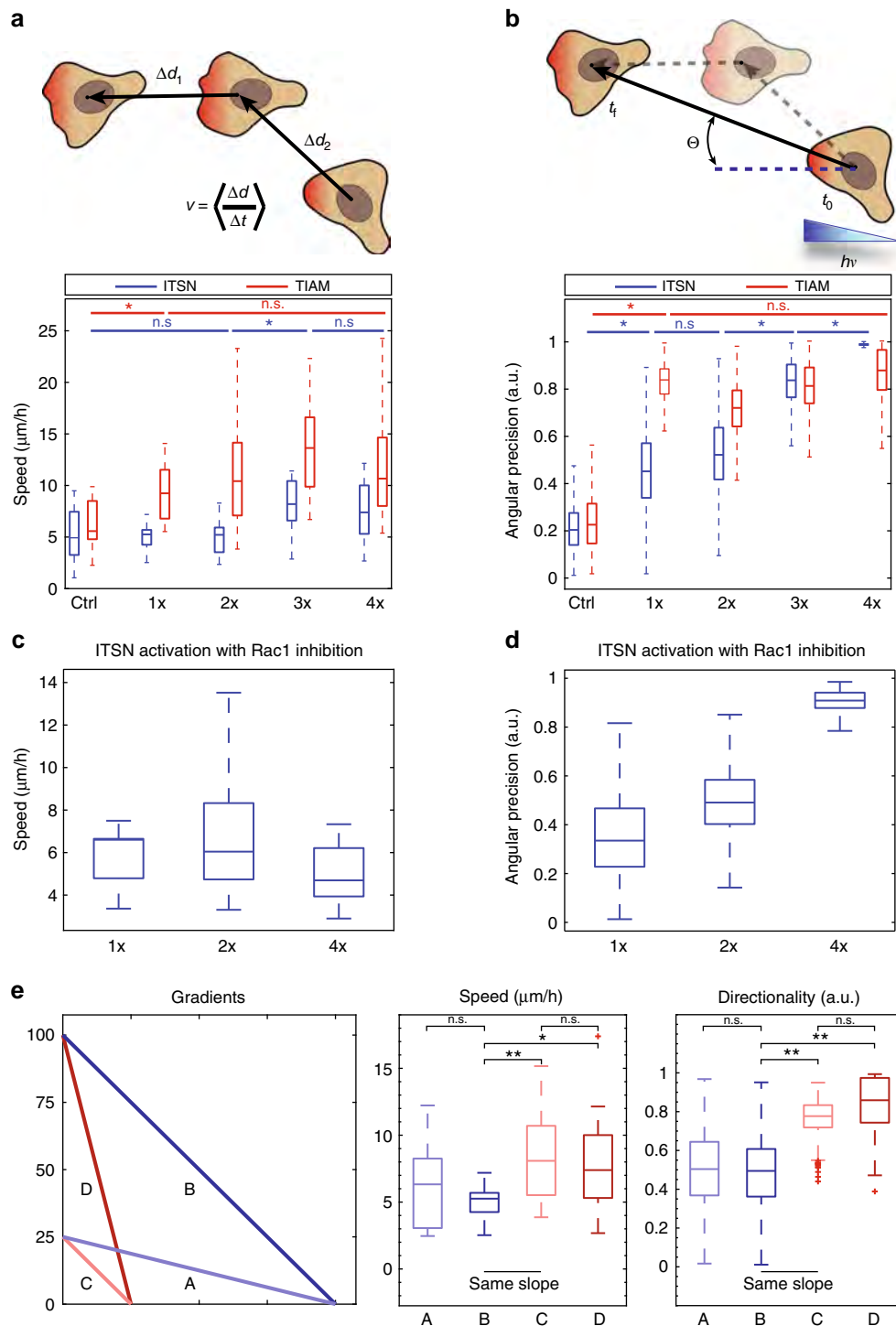
gradients of ITSN activation with different slopes but the same spatial extent, we could not detect any difference in cell motility (Fig. 6e). This also confirms that the amplitude of the imposed gradient itself does not affect the cellular response. Instead, when we imposed gradients of similar slope or amplitude but different extents, we could observe that cells stimulated with the shorter gradient of ITSN activation migrated with higher velocity and better orientation (Fig. 6e). These results indicate that the spatial extent is the critical parameter of Rho GTPase gradients read by cells.

Discussion

In this work, we observed that the front of randomly migrating cells presents an exponentially decaying Cdc42 activity gradient whereas Rac1 shows a complex shape peaking at approximately 6 μm from the cell edge, similarly to what has been observed before in other cell types^{9,36}. Combining experimental and model-based approaches, we could identify a network topology and map it spatially, allowing us to explain how these two distinct intracellular patterns are formed. By quantitatively tweaking the spatial patterns of specific GEF activity for either Cdc42 or Rac1 using optogenetics while quantifying the downstream recruitment of effectors, we showed that Cdc42 patterning can be simply explained by the combination of a localized GEF and a uniform GAP, but that Rac1 required a more complex circuitry.

We found that two mechanisms could account for Rac1 patterning. Combining one exponentially decaying GEF with either a GAP with a shorter exponential decay (like $\beta 2$ -chimaerin) or a directed transport from the cell front due to the actin retrograde flow was sufficient to recapitulate the observed Rac1 gradient. Yet, we showed that the effect of the actin retrograde flow does not act directly on Rac1 itself but is required for the front-most localization of $\beta 2$ -chimaerin. It has been previously demonstrated that the actin retrograde flow is coupled to cell polarity, by transporting various proteins away from the cell front⁵⁴. The actin flow could act on an inhibitor of $\beta 2$ -chimaerin. Another possibility is that $\beta 2$ -chimaerin localizes at the barbed end of actin filaments thanks to its interaction with the adaptor protein Nck1⁴⁸. Nck1 is also localized at the tip of migrating cells by the Gab1-NWASP complex⁵⁷. Since we additionally showed that a feedback from Rac1 leads to $\beta 2$ -chimaerin enrichment, $\beta 2$ -chimaerin recruitment would depend on two concomitant signals: a Rac1-dependent signal likely going through Rac1-dependent PKC-DAG production⁵⁸, and an actin polymerizing signal through the adaptor protein Nck1. This would also explain the crosstalk from Cdc42 to $\beta 2$ -chimaerin through N-WASP and an increase of Nck1-mediated $\beta 2$ -chimaerin recruitment.

Interestingly, Cdc42 and Rac1 gradients have similar exponential decays but different spatial extents due to the local inhibition of Rac1 activity at the cell front. This observation raises important questions about the way cells interpret signaling



gradients. Using quantitative optogenetics, we could directly control the spatial extent, slope or amplitude of intracellular activity gradients. We showed that cell migration is not determined by the amplitude or slope of Rho GTPase gradients, but rather by their spatial extent, similarly to what was proposed in a recent work on ERK morphogen gradients in *Drosophila* embryos⁵⁹. The spatial extent of Cdc42 needs to be small to ensure fine directionality in cell movement, in accordance with the previously shown role of Cdc42 as the primary conductor of chemotactic steering and cell polarity⁹. The spatial extent of Rac1 is larger, providing speed to the cell. Yet, since we could not effectively apply sharper Rac1 gradients without disrupting the

network topology, we do not know if the spatial extent of Rac1 presents a functional optimum as for Cdc42. Our approach can appear similar to the recent work of Zimmerman et al. who used optogenetic activations of Cdc42 and Rac1 to guide cell migration⁶⁰. However, in their work they imposed long-range light gradients to mimic external chemo-attractant gradients, whereas in our work we imposed subcellular light gradients to keep the cell and not the environment as the relevant spatial referential of Rho GTPase gradients.

In this study, we did not consider the temporal dynamics of Rho GTPase activities. While it is very likely that spatial and temporal dynamics are connected in freely migrating cells and

Fig. 6 Cdc42 and Rac1 drive different cellular responses. **a, b** Trajectories of cells stimulated as represented in Fig. 5 were analyzed quantitatively. **a** Cell speed defined as the instantaneous velocity of the cell displacement averaged over five consecutive time frames (top scheme). Box plots show instantaneous velocity of cells expressing CIBN-GFP-CAAX together with ITSN-CRY2-mCherry (blue) or TIAM-CRY2-mCherry (red) stimulated with various gradients of light (ITSN: $n = 25$ (ctrl), $n = 16$ (1×), $n = 20$ (2×), $n = 19$ (3×), $n = 16$ (4×), TIAM: $n = 19$ (ctrl), $n = 18$ (1×), $n = 18$ (2×), $n = 17$ (3×), $n = 18$ (4×)). Box plots represent the median, interquartile (box), 1.5 IQR (whiskers). **b** Directionality defined as the angular precision of cell displacement: the angle of displacement was measured using the initial position averaged over the first three frames and the final position averaged over the last three frames (top scheme). Angles were then bootstrapped and angular precision was calculated with the formula $r = \sqrt{(1/n^* \sum_{i=1}^n \sin \theta_i)^2 + (1/n^* \sum_{i=1}^n \cos \theta_i)^2}$. Box plots represent the median, interquartile (box), 1.5 IQR (whiskers). Statistical significance between consecutive conditions was evaluated using Wilcoxon's rank sum test. * $p \leq 0.05$. n.s., nonsignificant ($p > 0.05$). **c** Speed and **d** directionality measurements on HeLa cells expressing CIBN-GFP-CAAX and ITSN-CRY2-mCherry after Rac1 inhibition with 100 μM NSC 23766 and stimulated with various Cdc42 gradients. $n = 8$ (1×), $n = 16$ (2×) or $n = 17$ (4×). **e** Effects of slope, amplitude, and spatial extent of Cdc42 gradients on cell velocity and angular precision. HeLa cells expressing CIBN-GFP-CAAX and ITSN-CRY2-mCherry were stimulated with varying gradients of light. Gradients in blue (**a, b**) and red (**c, d**) have two distinct spatial extents. Gradients in light (**a, c**) and dark (**b, d**) color have two distinct amplitudes. Two gradients (**b, c**) have the same slope. $n = 13$ (**a**), $n = 16$ (**b**), $n = 22$ (**c**), $n = 16$ (**d**). * $p \leq 0.05$, ** $p \leq 0.01$, n.s., nonsignificant ($p > 0.05$) (Wilcoxon rank sum test)

while Rho GTPases patterns evolve on timescales of $\sim 100 \text{ s}^{19}$, the response functions we measured under our steady optogenetic activations did not show evolving spatiotemporal patterns (Supplementary Figure 4). Thus, even if our synthetic approach does not recapitulate the full spatiotemporal complexity seen in native cells, we can consider our results as an example of the signaling network capacity to respond to spatially modulated inputs. Given the similarity between the native and induced gradients of Rac1/Cdc42, we can be confident that the mechanisms we propose for gradient shaping are biologically relevant, at least at the coarse-grained cellular scale.

Following a correlative approach, Yamao et al. recently studied in time and space the patterns of Rac1 and Cdc42 activities and their link with the membrane dynamics in randomly migrating cells⁶¹. They concluded that Cdc42 induces random cell migration and Rac1 is responsible for persistent movement. While it might sound different from our results, the discrepancies might be explained by the scales and parameters observed in each case. We measure local and instantaneous quantities (speed and directionality), and Yamao and colleagues measure integrated and macroscopic ones (persistence and randomness). We were not able to measure those integrated quantities, since our optogenetic activations were not following the cells as they moved out of the adhesive micro-patterns. However, these different scales can be reconciled. As we conclude that Rac1 provides cells with higher speed, it also means long-term movement is more persistent^{54,62}. Similarly, since we show that sharp Cdc42 gradients can fine-tune directionality, local and transient Cdc42 pulses could steer cells randomly in complex trajectories.

The minimal circuitry that we identified as sufficient to shape Cdc42 and Rac1 gradients raises new unanswered questions. In particular, it is unclear how gradients of GEFs and GAPs are shaped throughout the cell, beside the formation of the $\beta 2$ -chimaerin gradient we identified. Our results suggest a role for the cytoskeleton itself and its dynamics to enrich $\beta 2$ -chimaerin at the cell border. More generally, actin networks and actin-regulating complexes can act as scaffolding complexes in protrusive regions where they localize. For example, the WAVE Complex, a downstream effector of Rac1, recruits WRP, a GAP inhibiting Rac1⁶³. Similarly, N-WASP, a downstream effector of Cdc42, associates with the GEF ITSN. More mechanisms are probably involved. In particular, membranes could play a direct role in the localization of these regulators of Rho GTPase activity. The local lipid composition, and in particular the concentration of PIP3, has been shown to control the activity of Rac1 and Cdc42^{26,28,64}. In addition, membrane curvature-sensing BAR proteins localize at highly bent membranes, including cell edges. Several BAR proteins are known to bind Rho GTPases or their regulators. IRSp53, a member of the I-BAR family found in

lamellipodia and filopodia has been shown to bind Cdc42, Rac1 and WAVE2^{65,66}. Even if $\beta 2$ -chimaerin was sufficient to explain Rac1 shaping in the present work, other known GAPs, such as ARHGAP22, ARHGAP24 (FILGAP) and SH3BP1, interact with the proteins involved in cell protrusion and could play a similar role as $\beta 2$ -chimaerin. In particular, it was previously shown that depletion of SH3BP1 results in a high activity of Rac1 at the front⁶⁷. Also, it remains to be explored if the Cdc42 and Rac1 positive feedbacks and crosstalks, as previously suggested⁹ and observed in our work (Fig. 3b), play a role in shaping GEF distributions.

Methods

Plasmids and molecular constructs. ITSN-CRY2-mCherry was constructed as detailed previously⁴⁴. The TIAM DH-PH domain was similarly amplified from TIAM(DHPPH)-Linker-YFP-PIF (gift from O. Weiner, University of California, San Francisco) and cloned into CRY2PHR-mCherry. Both ITSN-CRY2-mCherry and TIAM-CRY2-mCherry were cloned in pHR lentiviral vectors (gift from O. Weiner) by Genscript (Nanjing, China) using *MluI* and *BstBI* cloning sites. N-WASP-iRFP, PAK1-iRFP and $\beta 2$ -chimaerin-iRFP fusion genes were constructed by Genscript (Nanjing, China) by cloning the corresponding human cDNAs upstream the iRFP713 gene sequence⁶⁸, separated by a PVAT sequencer. The Abi1-iRFP plasmid was kindly provided by Maria Carla Parrini. Rac1BS and Cdc42BS plasmids were kindly provided by Dr. Louis Hodgson³⁵, and were subcloned into the lentiviral pLVX vector (Clontech, Mountain View, CA USA) between *XmaI* and *XbaI* cloning sites.

Cell culture and reagents. HeLa cells (CCL-2 strain, bought from ATCC) were cultured at 37 °C with 5% CO₂ in Dulbecco's modified Eagle's medium supplemented with 10% fetal bovine serum and penicillin-streptomycin (100 U/ml). Transfections were performed using X-tremeGENE 9 (Roche Applied Science, Penzberg, Bavaria, Germany) according to the manufacturer's instructions using an equal amount of plasmid DNA for each construct (1 μg). Stable cell lines were obtained using lentiviral infections: all lentiviruses were produced by transfecting pHR- or pLVX-based plasmids along with the vectors encoding packaging proteins (pMD2.G and psPax2) using HEK-293T cells. Viral supernatants were collected 2 days after transfection and HeLa cells were transduced at an MOI of 2. Gene expression knockdown was achieved using pooled siRNA with the following sequences. Cdc42: 5'-CGAUGGUGCUGUUGGUA-3' and 5'-CUAUGCAGUCACAGUUAUG-3', $\beta 2$ -chimaerin: 5'-AUUGAAGCAAGAGGAUUA-3' and 5'-CCACUCAAUUAUGAGAAG-3', Rac1: 5'-UUUACCUACAGUCUCCGUUUU-3' and 5'-UACAGCACCAUUCUUAUUU-3', ctrl: 5'-AGGUAGUUAUUGCCUUG-3' and 5'-GCGGGATATTTCCGGTCAAT-3'. siRNA transfection was done following the manufacturer's protocol (Lipofectamine RNAiMax, Thermo Fischer Scientific), and cells were imaged 48 h after transfection. The JLY cocktail (8 μM jasplakinolide, 5 μM Latrunculin B, 20 μM Y27632) was applied 15 min before image acquisition.

Live cell imaging and optogenetics. Micropatterned coverslips were prepared as described by Azioune et al.⁶⁹. O₂ plasma-cleaned coverslips were incubated with 0.1 mg/ml of PLL-g-PEG (Surface Solutions, Switzerland) in 10 mM HEPES, pH 7.4 for 1 h. They were then exposed to deep UV through micropatterned quartz/chrome photomasks (Toppan, Round Rock, TX) for 5 min, and incubated with fibronectin in 100 mM NaHCO₃ (pH 8.5) for 1 h. Releasable micropatterns were prepared similarly, with PLL-PEG being replaced by azido-PLL-g-PEG (APP) at 100 $\mu\text{g}/\text{ml}$. Migration was released by addition of 20 μM BCN-RGD for 10 min. Before imaging, cells were dissociated using Versene (Life Technologies) and

seeded for adhesion on the previously mentioned coverslips for at least 2 h. Experiments were performed at 37 °C in 5% CO₂ in a heating chamber (Pecon, Meyer Instruments, Houston, TX) placed on an inverted microscope model No. IX71 equipped with a ×60 objective with NA 1.45 (Olympus, Melville, NY) and a Luca R camera (Andor, Belfast, UK). The microscope was controlled with the Metamorph software (Molecular Devices, Eugene, OR). TIRF images were acquired using an azimuthal TIRF module (iLas2; Roper Scientific, Tucson, AZ). Optogenetics stimulations were performed every 30–40 s with a DMD in epi-mode (DLP Light Crafter, Texas Instruments) illuminated with a SPECTRA Light Engine (Lumencor, Beaverton, OR USA) at 440 ± 10 nm.

FRET. HeLa cells were lentivirus-infected with a Cdc42-FRET-biosensor or a Rac1-FRET-biosensor (kindly provided by Louis Hodgson) and sorted for intermediary fluorescence using fluorescence-activated cell sorting (FACS). Twenty-four hours after plating them on glass coverslips, cells were imaged by TIRF microscopy. Excitation was done with a laser at 405 nm, dichroic mirrors stayed the same (BS: FF-458-DiO2, Semrock) while a filterwheel allowed for the switching of appropriate emission filters to acquire sequentially donor (mCerulean, Em: FF01-483/32) and FRET (Em: FF01-542/27) emissions. Image processing included registration, flat-field correction, background subtraction, segmentation, and FRET/donor ratio calculations. FRET profiles measured from the FRET images were normalized between 0 and 1 when comparing the two Cdc42 and Rac1 FRET reporters or when comparing a FRET reporter with another fluorescence signal. We did not normalize FRET profiles from the same reporter when comparing two different experimental conditions.

Immunofluorescence microscopy. HeLa cells stably expressing a Rac1-FRET-biosensor were fixed in phosphate buffer saline (PBS) with 4% paraformaldehyde for 20 min at 25 °C. After permeabilization in PBS + 0.1% Triton X-100 for 15 min and blocking in PBS + 1% BSA + 1% FBS for 20 min, stainings were performed in PBS with 0.05% Triton + 1% BSA 1 h at room temperature. Antibodies were used as follows: β2-chimaerin primary antibody: 1/100 (Orb182594, Biorbyt), anti-rabbit-Alexa594 antibody: 1/400 (ThermoFisher). Phalloidin-488 was used at 300 nM. Acquisitions were made in HiLo mode using an azimuthal TIRF module as described above.

Image processing and quantification of intracellular gradients. Images were analyzed with custom-built Matlab routines. For the images obtained in our optogenetic experiments, we subtracted the initial pre-optogenetics signal from all subsequent images in order to measure solely the recruitment of fluorescent proteins to the basal membrane and to avoid volume artifacts. The resulting differential images were normalized between 0 and 1 using the same normalizing factors as the gradients quantified from each image (see below). Normalized images were then averaged over ten time points and over all cells to produce the averaged images shown in Figs. 2d, f and 3b, d. The associated Fire color scale was defined as the average temporal fold change of fluorescence that we measured from the raw images after background subtraction (taken outside the cell mask). For the quantification of the gradients presented in Figs. 1b, and 3c, f, g, we measured the FRET ratio along two linescans per cell, drawn manually perpendicular to the cell edge in protrusive regions with a line width of 10 pixels. The gradients were first averaged for each cell, and then averaged over all cells. For the quantification of the gradients presented in Figs. 2b, e, g and 3e, h, i, fluorescence was quantified along a line of 10 pixels in width spanning across the cell diameter in the direction of the optogenetic gradients. The curves in Figs. 2b, e, g and 3e, h, i were normalized between 0 and 1 where 0 stands for the average of the five minimal values and 1 stands for the average of the five maximal fluorescence values.

Processing of the migration movies. Movies were analyzed with custom-built Matlab routines. The segmentation of cell borders was performed on fluorescence images using the Matlab function Graythresh. Cell centroid positions were determined using the Matlab function Regionprops and used to quantify cell movement. To measure cell velocity, we computed instantaneous speed of cell centroids at each time frame, and then averaged it over several time frames. Cells stimulated through TIAM activation reached maximum speed soon after the beginning of illumination, so instantaneous speed was averaged between $t = 15$ min to $t = 45$ min. Cells stimulated through ITSN activation reached maximum speed at later stages, and instantaneous speed was thus averaged between $t = 60$ min to $t = 90$ min. Angular precision was computed as follows: for each cell, the displacement vector was computed between the initial cell centroid (averaged over the three first time frames) and the final cell centroid (averaged over the three last time frames), and we measured the angle between this vector and the axis of stimulation gradients. These angles were bootstrapped over 1000 replications, and angular precision was estimated with the formula

$$p = \sqrt{\left(\frac{1}{n^*} \sum_{i=1}^n \sin \theta_i \right)^2 + \left(\frac{1}{n^*} \sum_{i=1}^n \cos \theta_i \right)^2}. \text{ The morphodynamics maps}$$

(Fig. 5c) were obtained using a routine adapted from Yang⁹. The cell contour was aligned such that the middle of the map was centered on the direction imposed by the optogenetic gradient.

Data availability

The data that support the findings of this study and all custom codes used for analysis are available from the corresponding author upon reasonable request.

Received: 3 April 2018 Accepted: 19 October 2018

Published online: 16 November 2018

References

1. Van Haastert, P. J. M. & Devreotes, P. N. Chemotaxis: signalling the way forward. *Nat. Rev. Mol. Cell Biol.* **5**, 626–634 (2004).
2. Weiner, O. D. et al. Hem-1 complexes are essential for Rac activation, actin polymerization, and myosin regulation during neutrophil chemotaxis. *PLoS Biol.* **4**, 186–199 (2006).
3. Bray, D. Axonal growth in response to experimentally applied mechanical tension. *Dev. Biol.* **102**, 379–389 (1984).
4. Choquet, D., Felsenfeld, D. P. & Sheetz, M. P. Extracellular matrix rigidity causes strengthening of integrin–cytoskeleton linkages. *Cell* **88**, 39–48 (1997).
5. Pelham, R. J. & Wang, Y. L. Cell locomotion and focal adhesions are regulated by the mechanical properties of the substrate. *Biol. Bull.* **194**, 348–350 (1998).
6. McCarthy, J. B., Palm, S. L. & Furcht, L. T. Migration by haptotaxis of a schwann-cell tumor line to the basement-membrane glycoprotein laminin. *J. Cell. Biol.* **97**, 772–777 (1983).
7. Weber, M. et al. Interstitial dendritic cell guidance by haptotactic chemokine gradients. *Science* **339**, 328–332 (2013).
8. Huang, C.-H., Tang, M., Shi, C., Iglesias, Pa & Devreotes, P. N. An excitable signal integrator couples to an idling cytoskeletal oscillator to drive cell migration. *Nat. Cell Biol.* **15**, 1307–1316 (2013).
9. Yang, H. W., Collins, S. R. & Meyer, T. Locally excitable Cdc42 signals steer cells during chemotaxis. *Nat. Cell Biol.* **18**, 191–201 (2015).
10. van Haastert, P. J. M., Keizer-Gunnink, I. & Kortholt, A. Coupled excitable Ras and F-actin activation mediates spontaneous pseudopod formation and directed cell movement. *Mol. Biol. Cell* **28**, 922–934 (2017).
11. Nobes, C. D. & Hall, A. Rho, rac, and cdc42 GTPases regulate the assembly of multimolecular focal complexes associated with actin stress fibers, lamellipodia, and filopodia. *Cell* **81**, 53–62 (1995).
12. Nobes, C. D. & Hall, A. Rho GTPases control polarity, protrusion, and adhesion during cell movement. *J. Cell Biol.* **144**, 1235–1244 (1999).
13. Ridley, A. J. et al. Cell migration: integrating signals from front to back. *Science* **302**, 1704–1709 (2003).
14. Peng, J., Wallar, B. J., Flanders, A., Swiatek, P. J. & Alberts, A. S. Disruption of the Diaphanous-related formin Drf1 gene encoding mDia1 reveals a role for Drf3 as an effector for Cdc42. *Curr. Biol.* **13**, 534–545 (2003).
15. Svitkina, T. M. & Borisy, G. G. Progress in protrusion: the tell-tale scar. *Trends Biochem. Sci.* **24**, 432–436 (1999).
16. Raftopoulos, M. & Hall, A. Cell migration: rho GTPases lead the way. *Dev. Biol.* **265**, 23–32 (2004).
17. Burrridge, K. & Wennerberg, K. Rho and Rac take center stage. *Cell* **116**, 167–179 (2004).
18. Pertz, O., Hodgson, L., Klemke, R. L. & Hahn, K. M. Spatiotemporal dynamics of RhoA activity in migrating cells. *Nature* **440**, 1069–1072 (2006).
19. Machacek, M. et al. Coordination of Rho GTPase activities during cell protrusion. *Nature* **461**, 99–103 (2009).
20. Aspenstrom, P., Fransson, A. & Saras, J. Rho GTPases have diverse effects on the organization of the actin filament system. *Biochem. J.* **377**, 327–337 (2004).
21. Kitzing, T. M. et al. Positive feedback between Dia1, LARG, and RhoA regulates cell morphology and invasion. *Genes Dev.* **21**, 1478–1483 (2007).
22. Bishop, A. L. & Hall, A. Rho GTPases and their effector proteins. *Biochem. J.* **348**(Pt 2), 241–255 (2000).
23. Bos, J. L., Rehmann, H. & Wittinghofer, A. GEFs and GAPs: critical elements in the control of small G proteins. *Cell* **129**, 865–877 (2007).
24. Dovas, A. & Couchman, J. R. RhoGDI: multiple functions in the regulation of Rho family GTPase activities. *Biochem. J.* **390**, 1–9 (2005).
25. Hodgson, L. et al. FRET binding antenna reports spatiotemporal dynamics of GDI-Cdc42 GTPase interactions. *Nat. Chem. Biol.* **12**, 802–809 (2016).
26. Aoki, K., Nakamura, T., Fujikawa, K. & Matsuda, M. Local phosphatidylinositol 3,4,5-trisphosphate accumulation recruits Vav2 and Vav3 to activate Rac1/Cdc42 and initiate neurite outgrowth in nerve growth factor-stimulated PC12 cells. *Mol. Biol. Cell* **16**, 2207–2217 (2005).
27. Karunaratne, W. K. A., Giri, L., Patel, A. K., Venkatesh, K. V. & Gautam, N. Optical control demonstrates switch-like PIP3 dynamics underlying the initiation of immune cell migration. *Proc. Natl. Acad. Sci. USA* **110**, E1575–E1583 (2013).
28. Weiner, O. D. et al. A PtdInsP(3)- and Rho GTPase-mediated positive feedback loop regulates neutrophil polarity. *Nat. Cell Biol.* **4**, 509–513 (2002).

29. Brown, G. C. & Kholodenko, B. N. Spatial gradients of cellular phospho-proteins. *FEBS Lett.* **457**, 452–454 (1999).
30. Bement, W. M., Miller, A. L. & Von Dassow, G. Rho GTPase activity zones and transient contractile arrays. *Bioessays* **28**, 983–993 (2006).
31. Fritz, R. D. & Pertz, O. The dynamics of spatio-temporal Rho GTPase signaling: formation of signaling patterns. *Fluorescence* **5**, 749–761 (2016).
32. Fusco, L. et al. Computer vision profiling of neurite outgrowth dynamics reveals spatiotemporal modularity of Rho GTPase signaling. *J. Cell Biol.* **212**, 91–111 (2016).
33. Pertz, O. Spatio-temporal Rho GTPase signaling—where are we now? *J. Cell Sci.* **123**, 1841–1850 (2010).
34. Vicente-Manzanares, M., Newell-Litwa, K., Bachir, A. I., Whitmore, L. A. & Horwitz, A. R. Myosin IIA/IIB restrict adhesive and protrusive signaling to generate front-back polarity in migrating cells. *J. Cell Biol.* **193**, 381–396 (2011).
35. Hanna, S., Miskolci, V., Cox, D. & Hodgson, L. A new genetically encoded single-chain biosensor for Cdc42 based on FRET, useful for live-cell imaging. *PLoS ONE* **9**, e96469 (2014).
36. Johnsson, A. K. E. et al. The Rac-FRET mouse reveals tight spatiotemporal control of Rac activity in primary cells and tissues. *Cell Rep.* **6**, 1153–1164 (2014).
37. Grimm, O., Coppey, M. & Wieschaus, E. Modelling the Bicoid gradient. *Development* **137**, 2253–2264 (2010).
38. Ben-Zvi, D., Shilo, B., Fainsod, A. & Barkai, N. Scaling of the BMP activation gradient in *Xenopus* embryos. *Nature* **453**, 1205–1211 (2008).
39. Plouhinec, J., Zakin, L., Moriyama, Y. & De Robertis, E. M. Chordin forms a self-organizing morphogen gradient in the extracellular space between ectoderm and mesoderm in the *Xenopus* embryo. *Proc. Natl Acad. Sci. USA* **110**, 20372–20379 (2013).
40. Kennedy, M. J. et al. Rapid blue-light-mediated induction of protein interactions in living cells. *Nat. Methods* **7**, 973–975 (2010).
41. Levskaya, A., Weiner, O. D., Lim, W. A. & Voigt, C. A. Spatiotemporal control of cell signalling using a light-switchable protein interaction. *Nature* **461**, 1–5 (2010).
42. Sakai, S., Ueno, K., Ishizuka, T. & Yawo, H. Parallel and patterned optogenetic manipulation of neurons in the brain slice using a DMD-based projector. *Neurosci. Res.* **75**, 59–64 (2013).
43. They, M. et al. Anisotropy of cell adhesive microenvironment governs cell internal organization and orientation of polarity. *Proc. Natl Acad. Sci. USA* **103**, 19771–19776 (2006).
44. Valon, L. et al. Predictive spatiotemporal manipulation of signaling perturbations using optogenetics. *Biophys. J.* **109**, 1785–1797 (2015).
45. Guilluy, C., Garcia-Mata, R. & Burridge, K. Rho protein crosstalk: another social network? *Trends Cell Biol.* **21**, 718–726 (2011).
46. Innocenti, M. et al. Abi1 regulates the activity of N-WASP and WAVE in distinct actin-based processes. *Nat. Cell Biol.* **7**, 969–976 (2005).
47. Dang, I. et al. Inhibitory signalling to the Arp2/3 complex steers cell migration. *Nature* **503**, 281–284 (2013).
48. Gutierrez-Uzquiza, A. et al. Coordinated activation of the Rac-GAP β 2-chimaerin by an atypical proline-rich domain and diacylglycerol. *Nat. Commun.* **4**, 1849 (2013).
49. Peng, G. E., Wilson, S. R. & Weiner, O. D. A pharmacological cocktail for arresting actin dynamics in living cells. *Mol. Biol. Cell* **22**, 3986–3994 (2011).
50. Van Dongen, S. F. M., Maiuri, P., Marie, E., Tribet, C. & Piel, M. Triggering cell adhesion, migration or shape change with a dynamic surface coating. *Adv. Mater.* **25**, 1687–1691 (2013).
51. Etienne-Manneville, S. & Hall, A. Integrin-mediated activation of Cdc42 controls cell polarity in migrating astrocytes through PKC ζ . *Cell* **106**, 489–498 (2001).
52. Yang, L., Wang, L. & Zheng, Y. Gene targeting of Cdc42 and Cdc42GAP affirms the critical involvement of Cdc42 in filopodia induction, directed migration, and proliferation in primary mouse embryonic fibroblasts. *Mol. Biol. Cell* **17**, 4675–4685 (2006).
53. Pankov, R. et al. A Rac switch regulates random versus directionally persistent cell migration. *J. Cell Biol.* **170**, 793–802 (2005).
54. Maiuri, P. et al. Actin flows mediate a universal coupling between cell speed and cell persistence. *Cell* **161**, 374–386 (2015).
55. Morel, M. et al. Amplification and temporal filtering during gradient sensing by nerve growth cones probed with a microfluidic assay. *Biophys. J.* **103**, 1648–1656 (2012).
56. Andrew, N. & Insall, R. H. Chemotaxis in shallow gradients is mediated independently of PtdIns 3-kinase by biased choices between random protrusions. *Nat. Cell Biol.* **9**, 193–200 (2007).
57. Abella, J. V. et al. The Gab1 scaffold regulates RTK-dependent dorsal ruffle formation through the adaptor Nck. *J. Cell Sci.* **123**, 1306–1319 (2010).
58. Yang, C. & Kazanietz, M. G. Chimaerins: GAPs that bridge diacylglycerol signalling and the small G-protein Rac. *Biochem. J.* **403**, 1–12 (2007).
59. Johnson, H. E. et al. The spatiotemporal limits of developmental Erk signaling. *Dev. Cell* **40**, 185–192 (2017).
60. Zimmerman, S. P., Asokan, S. B., Kuhlman, B. & Bear, J. E. Cells lay their own tracks—optogenetic Cdc42 activation stimulates fibronectin deposition supporting directed migration. *J. Cell Sci.* **130**, 2971–2983 (2017).
61. Yamao, M. et al. Distinct predictive performance of Rac1 and Cdc42 in cell migration. *Sci. Rep.* **5**, 17527 (2015).
62. Maiuri, P. et al. The first world cell race. *Curr. Biol.* **22**, R673–R675 (2012).
63. Soderling, S. H. et al. The WRP component of the WAVE-1 complex attenuates Rac-mediated signalling. *Nat. Cell Biol.* **4**, 970–975 (2002).
64. Jin, T. Gradient sensing during chemotaxis. *Curr. Opin. Cell Biol.* **25**, 532–537 (2013).
65. Connolly, B. A., Rice, J., Feig, L. A. & Buchsbaum, R. J. Tiam1-IRS53 complex formation directs specificity of rac-mediated actin cytoskeleton regulation. *Mol. Cell Biol.* **25**, 4602–4614 (2005).
66. Zhao, H., Pykäläinen, A. & Lappalainen, P. I-BAR domain proteins: linking actin and plasma membrane dynamics. *Curr. Opin. Cell Biol.* **23**, 14–21 (2011).
67. Parrini, M. C. et al. SH3BP1, an exocyst-associated RhoGAP, inactivates Rac1 at the front to drive cell motility. *Mol. Cell* **42**, 650–661 (2011).
68. Filonov, G. S. et al. Bright and stable near-infrared fluorescent protein for in vivo imaging. *Nat. Biotechnol.* **29**, 757–761 (2011).
69. Azioune, A., Storch, M., Bornens, M., They, M. & Piel, M. Simple and rapid process for single cell micro-patterning. *Lab. Chip* **9**, 1640–1642 (2009).

Acknowledgements

We thank Louis Hodgson for sharing the Rho GTPase sensors; Maria Carla Parrini, Kristine Schauer, and Christophe Tribet for critical reading of the manuscript and helpful discussions; Remy Fert and Eric Nicolau for their technical assistance; The Institut Curie Shared FACS Facility for cell sorting. M.C. acknowledges financial support from French National Research Agency (LICOP no. ANR-12-JSV5-0002-01). M.C. and M.D. acknowledge funding from French National Research Agency (ANR) Paris-Science-Lettres Program (ANR-10-IDEX-0001-02 PSL), Labex CeTisPhyBio (No. ANR-10-LBX-0038), the France-BioImaging infrastructure supported by ANR Grant ANR-10-INSB-04 (Investments for the Future), and Institut Pierre-Gilles de Gennes (laboratoire d'excellence, Investissements d'Avenir program ANR-10-IDEX-0001-02 PSL and ANR-10-LABX-31).

Author contributions

Conceptualization, S.D.B., M.D. and M.C.; Methodology, S.D.B., M.D. and M.C.; Software, S.D.B. and M.C.; Formal analysis, S.D.B., K.V. and M.C.; Investigation, S.D.B., K.V. and J.M.; Resources, F.d.F., G.C., and F.D.; Writing—original draft, S.D.B. and M.C.; Writing—review and editing, S.D.B., M.C., M.D. and K.V.; Visualization, S.D.B. and K.V.; Supervision, M.C.; Funding acquisition, M.C.

Additional information

Supplementary Information accompanies this paper at <https://doi.org/10.1038/s41467-018-07286-8>.

Competing interests: The authors declare no competing interests.

Reprints and permission information is available online at <http://npg.nature.com/reprintsandpermissions/>

Publisher's note: Springer Nature remains neutral with regard to jurisdictional claims in published maps and institutional affiliations.

 **Open Access** This article is licensed under a Creative Commons Attribution 4.0 International License, which permits use, sharing, adaptation, distribution and reproduction in any medium or format, as long as you give appropriate credit to the original author(s) and the source, provide a link to the Creative Commons license, and indicate if changes were made. The images or other third party material in this article are included in the article's Creative Commons license, unless indicated otherwise in a credit line to the material. If material is not included in the article's Creative Commons license and your intended use is not permitted by statutory regulation or exceeds the permitted use, you will need to obtain permission directly from the copyright holder. To view a copy of this license, visit <http://creativecommons.org/licenses/by/4.0/>.

© The Author(s) 2018